CRYSTAL GROWTH & DESIGN

pubs.acs.org/crystal

Article

Systematic Characterization of Naproxen Diastereomeric Salts with Cinchona Alkaloids toward Naproxen Resolution: Insights from a Multidisciplinary Approach

Patrizia Rossi, Meriem Goudjil, Martina Lippi,* Jacopo Ceccarelli, Samuele Ciattini, Luca Conti, Andrea Ienco, Juliana Morais Missina, and Paola Paoli

Cite This: *Cryst. Growth Des.* 2026, 26, 955−969

Read Online

ACCESS | Metrics & More | Article Recommendations | Supporting Information

ABSTRACT: The solid forms of three new diastereomeric quinine-based salts (two hydrated naproxen salts (**S-Nap_RS-Quin_W** and **R-Nap_RS-Quin_W**) and one anhydrous ibuprofen salt (**S-Ibu_RS-Quin**) were investigated using a combination of experimental techniques (e.g., X-ray diffraction, thermal analyses, infrared spectroscopy) and in silico methods. Additionally, the solid-state form of a naproxen-cinchonine salt (**S-Nap_SR-Cinch**) was studied, and for comparison, the crystal structure of a related quinine-based salt with flurbiprofen (**R-Fbu_RR-Quin**) was included. Structural characterization and phase stability studies, including hydration and dehydration behavior, offered valuable insights into the stability profiles of these compounds. Detailed in silico analyses further clarified the molecular interactions and packing arrangements underlying the solid-state structures. Together, these results provide a structural explanation for the enantioselective crystallization observed, highlighting the superior intrinsic stability of the **S-Nap_RS-Quin_W** crystal packing as a key factor driving chiral discrimination. This integrated approach advances our understanding of the molecular determinants that govern selective salt formation, with potential implications for the design of improved chiral separation strategies in pharmaceutical development.

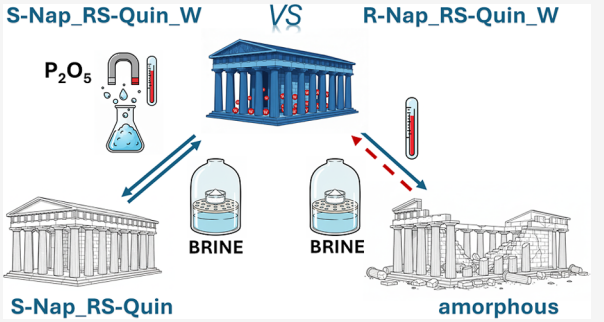

INTRODUCTION

About half of the synthetic drugs used nowadays are chiral compounds, containing at least one chiral center.[1] When just one of the two enantiomers of a racemic compound is the active one (eutomer), while the other is inactive or bioinert (distomer), the drug can be used as a racemic API (Active Pharmaceutical Ingredient).[2] But, if the distomer can cause undesired effects or it is toxic, as for example in the well-known case of thalidomide,[3] the use of the only eutomer is crucial.

Even if the distomer is not harmful, using only the active enantiomer is generally preferred, as it increases the API's efficiency and can reduce the required dosage for patients. Therefore, strategies for producing enantiopure APIs have been widely investigated. These procedures must be efficient and cost-effective and possibly based on green chemistry principles.[4,5] The most employed methods for obtaining single enantiomer samples principally include asymmetric synthesis, chromatographic resolution, kinetic resolution, and crystallization resolution. The latter approach relies on the crystallization of diastereomeric salts,[6−10] which is one of the most used techniques on a large or industrial scale,[11] or the synthesis of diastereomeric cocrystals[12,13] as well as on preferential crystallization.[14,15]

In the first two cases, considering that optical isomers have identical physical properties (such as melting and boiling points, density, solubility etc.) and differ only in reaction with chiral compounds, the use of an optically active resolving agent is needed, enabling the formation of diastereomeric salts or cocrystals whose different solubility allows the separation of the two enantiomers.[16,17] Resolution via diastereomeric salt crystallization is highly valued in the pharmaceutical industry due to its low cost and the ability to recover the resolving agent. However, selecting the optimal agent and experimental conditions remains largely empirical and time-consuming. Systematic studies of structurally related salts can move beyond the traditional trial-and-error approach by identifying key intermolecular interactions and structural features. Such insights streamline the selection process, providing a more rational basis for successful resolutions.

Received: October 30, 2025
Revised: December 24, 2025
Accepted: December 24, 2025
Published: January 8, 2026

As part of our research on the structure/physicochemical properties relationships[18,19] of different classes of APIs (β-blockers,[20,21] Nonsteroidal Anti-Inflammatory Drugs (NSAIDs),[22−24] dapsone structurally related molecules),[25,26] in the last years, we have concentrated our attention on the study of chiral resolution by crystallization of NSAIDs belonging to the arylpropionic acid derivatives class,[10,27] characterized by a chiral center on the α-carbon of the propionic acid moiety.

To this group of drugs belong the well-known ibuprofen ((±)-2-(4-isobutylphenyl)propanoic acid) and ketoprofen ((±)-2-(3-benzoylphenyl)propanoic acid) as well as naproxen ((±)-2-(6-methoxynaphthalen-2-yl)propanoic acid) (see Scheme 1), which is the compound investigated in the present article.

Scheme 1. Chemical Formula of (a) Quinine, (b) Cinchonine, (c) Naproxen, (d) Ibuprofen, (e) Flurbiprofen, and (f) Ketoprofen (In the Quinine and Cinchonine Formulae, the Considered Chiral Centers Are Highlighted)

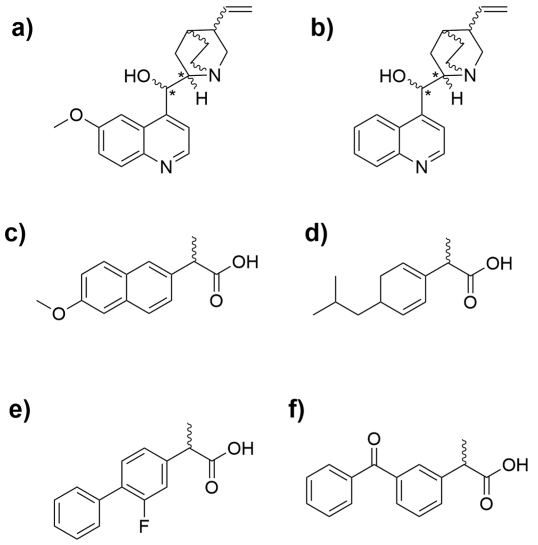

Naproxen, introduced in 1976 and currently the second most prescribed NSAID after ibuprofen,[28] is widely used as an analgesic, anti-inflammatory, and antipyretic agent for conditions such as arthritis, gout, and dysmenorrhea,[29−31] acting through the inhibition of both COX-1 and COX-2 enzymes[32]

Hence, except for naproxen, whose *R* enantiomer is hepatotoxic,[30,33] all these drugs are usually administered as racemic mixtures.[34] In fact, although the *S* enantiomers are the eutomers and act as API, the *R* distomers invert to the eutomer during metabolism via thio−esterase activity.[35,36] However, driven by factors such as lower toxicity and improved pharmacokinetics[37] recent years have seen a broad "chiral switch," in which racemic APIs are replaced by their single active enantiomers. Ibuprofen and ketoprofen were among the first to undergo this transition,[38,39] and their *S*-enantiomers are now included in several fixed-dose combination products, reinforcing the demand for efficient methods to access the enantiopure solid form. In this context, diastereomeric crystallization has emerged as a widely established and industrially viable approach for resolving racemic mixtures relying on the different solubility profiles of the resulting diastereomeric salts. In line with this, our recent work has focused on elucidating the enantioseparation of arylpropionic acid-based NSAIDs through the formation and selective crystallization of such salts using structurally diverse chiral resolving agents. As illustrative cases, we employed (*S*)-(−)-1-phenylethylamine[27] as an initial resolving agent, followed by *cis*-1-amino-2-indanol,[10] the latter introducing an additional stereocenter. The aim of this research was to integrate experimental and computational approaches to clarify the mechanisms governing chiral discrimination in the diastereomeric salts of NSAID anions. The purpose of these studies was to clarify the mechanisms governing both the formation and solid-state stability of the diastereomeric salts, thereby revealing how these processes contribute to any chiral discrimination observed. By combining advanced crystallographic methods (SCXRD, PXRD, and in situ studies), thermoanalytical techniques (DSC, TGA, and HSM), and in silico tools such as modeling and data mining, we characterized the solid forms of these salts and established clear links between their molecular organization and solid-state properties. Central to this analysis was the role of the hydrogen-bond network and other noncovalent interactions, which dictate structural stability, solubility, and ultimately selective crystallization. Together, these insights underscore the importance of crystallographic characterization in understanding the resolution efficiency and provide a mechanistic foundation for the rational design of resolving agents tailored to the stereochemical features of specific racemates.

As a further step in our investigation, we explored here naproxen diastereomeric salts with a more complex resolving agent, characterized by the presence of more than two stereogenic centers and a bulky molecular structure.

Our attention was drawn to naturally occurring alkaloids, which have long been among the most widely used resolving agents for chiral acids.[40]

Quinine, denoted here as RS-Quinine (for stereochemistry, see Scheme 1a), and cinchonine (SR-Cinchonine, Scheme 1b) are abundant alkaloids extracted from *Cinchona* bark. Extensively used in the chemical and pharmaceutical industries, quinine is a classic antimalarial but also finds applications in treating diabetes,[41,42] dengue virus,[43] and nocturnal leg cramps.[44] Its characteristic bitterness also makes it a common flavoring agent in beverages.[45] Beyond its medicinal properties, quinine's four stereocenters make it a versatile chiral resolving agent.[46] Historically, its derivative quinicine was instrumental in Pasteur's pioneering work on molecular chirality.[47] Similarly, the related alkaloid cinchonidine enabled the first large-scale production of enantiopure *S*-Naproxen.[46,48,49]

Interestingly, although the use of quinine as resolving agent for racemic acids is well established, only one article has been found concerning the use of a quinine-terminated tetra-arm PEGs in the chiral resolution of R- and S-Ibuprofen;[50] in addition in the Cambridge Structural Database (CSD, v. 5.46, update February 2025),[51] just one structure of a NSAID/quinine salt is reported (refcode: **IGATOC**, Flurbiprofen/RR-Quinine diastereomeric salt, **R-Fbu_RR-Quin** in the following).[52]

We thus, with the aim to obtain insight into the distinct molecular packing and intermolecular interactions that could facilitate enantiomeric separation, undertook a systematic investigation of some NSAIDs/*Cinchona* alkaloids salts. In fact, in addition to RS-Quinine, also salts made of RR-Quinine and SR-Cinchonine were studied, considering that both alkaloids can be regarded as diastereomers of RS-Quinine with respect to their stereogenic centers.

Herein, we report the results of the experimental and in silico investigation of the solid forms of three new quinine-based

https://doi.org/10.1021/acs.cgd.5c01538
Cryst. Growth Des. 2026, 26, 955−969

diastereomeric salts: the hydrated **S-Nap_RS-Quin_W** three hydrate salt and **R-Nap_RS-Quin_W** three hydrate salt and the anhydrous **S-Ibu_RS-Quin** salt. The study was further extended to the solid-state characterization of salt **S-Nap_SR-Cinch**, formed by (S)-(+)-Naproxen and SR-Cinchonine. Finally, the crystal structure of **R-Fbu_RR-Quin** was included in the study for comparative purposes. In addition, the thermal stability of the synthesized compounds and related solid forms was assessed by variable temperature powder diffraction (VT-PXRD), differential scanning calorimetry (DSC), thermal gravimetry (TGA), and hot-stage microscopy (HSM). Hydration and dehydration experiments, as well as a preliminary selective crystallization test, were carried out, and an in-depth in silico investigation was performed with the aim of extracting useful information about the factors governing the chiral separation. In particular, although these diastereomeric salts share a remarkably robust columnar hydrogen-bonding synthon, they exhibit clear differences in structural and thermal stabilities, most pronounced in the S- and R-Naproxen/RS-Quinine hydrates. The clear preference of the *S*-enantiomer for forming a stable, reversible channel hydrate, in contrast with the instability and amorphization of the corresponding R-hydrate, provides a compelling structural rationale for the observed selectivity in crystallization. By establishing these fundamental links among supramolecular organization, hydrate stability, and enantioselective crystallization behavior, this work offers crucial insights that can inform the rational selection and design of resolving agents for efficient large-scale production of enantiopure APIs.

EXPERIMENTAL SECTION

Chemicals

(S)-(+)-Naproxen (99%) and (R)-(+)-Naproxen (96%) were purchased from Alfa Aesar, while (S)-(+)-Ibuprofen (99%) was purchased from Sigma-Aldrich. RS-Quinine and SR-Cinchonine were purchased from Alfa Aesar. Deionized water and ethanol (99%) were purchased from Sigma-Aldrich. All of the reagents and solvents were used as received without further purification.

Salt Preparation

All syntheses were performed in solution by using deionized water and 99% ethanol. **S-Nap_RS-Quin_W** three hydrate and **S-Ibu_RS-Quin** salts were obtained both as single crystals (SCs) and as microcrystalline powders (MPs) under atmospheric conditions. A microcrystalline phase of the **R-Nap_RS-Quin_W** three hydrate salt was obtained from R-naproxen and RS-Quin; attempts to obtain single crystals were unsuccessful (details in the Supporting Information, Table S1). Finally, the **S-Nap_SR-Cinch** salt was obtained exclusively as single crystals requiring the heating of the solution. Attempts to reproduce its microcrystalline phase were carried out without any success (Table S2).

Preparation of S-Nap_RS-Quin_W. *Synthesis of SCs.* In a test tube, S-Naproxen (230.3 mg, 1 mmol) and RS-Quinine (324.4 mg, 1 mmol) were dissolved in 5 mL of ethanol (EtOH). Then, 1 mL of water was added, and the solution was allowed to slowly evaporate (at room temperature), allowing the formation of SCs after a couple of days.

Synthesis of MPs. S-Naproxen (230.3 mg, 1 mmol) was dissolved in 5 mL of EtOH and RS-Quinine (324.4 mg, 1 mmol) was added to the solution, followed by the addition of 4 mL of water. Instantly, a white solid started to form. Then, the resulting precipitate was collected by filtration and was analyzed by powder X-ray diffraction (PXRD). The obtained PXRD pattern was compared to the simulated one derived from the **S-Nap_RS-Quin_W** single-crystal data, confirming the formation of the same crystalline phase (see Figure S1).

Preparation of R-Nap_RS-Quin_W. *Synthesis of MPs.* R-Naproxen (230.3 mg, 1 mmol) was dissolved in 5 mL of EtOH, and then 1 equiv of RS-Quinine (324.4 mg) was added. 4 mL of water was added to the solution, and a precipitate started to form. The solid was collected by filtration, dried, and analyzed by PXRD (Figure S2a).

Preparation of S-Ibu_RS-Quin. *Synthesis of SCs.* An equimolar amount of S-Ibuprofen (206.3 mg, 1 mmol) and RS-Quinine (324.4 mg, 1 mmol) in 10 mL of an ethanol/water (4:1) solution was left under slow evaporation at room temperature. After ca. 4 days, single crystals were formed.

Synthesis of MPs. S-Ibuprofen (1 mmol, 206.3 mg) and RS-Quinine (1 mmol, 324.4 mg) were dissolved in 6 mL of ethanol. After stirring for 30 min, 4 mL of water was added to the solution, leading to the formation of a white precipitate. The solid was collected by filtration and analyzed using PXRD. The obtained PXRD pattern was then compared to the simulated pattern derived from the **S-Ibu_RS-Quin** single-crystal data, confirming the formation of the same crystalline phase (see Figure S3).

Preparation of S-Nap_SR-Cinch. *Synthesis of SCs.* In a test tube, S-Naproxen (230.3 mg, 1 mmol) and SR-Cinchonine (294.4 mg, 1 mmol) were suspended in 12 mL of an ethanol/water (3:1) solution. The mixture was stirred and heated to 80 °C until the complete dissolution of the solid. The solution was then cooled to room temperature and allowed to evaporate slowly. After a few days, single crystals formed.

Single-Crystal X-ray Diffraction (SC-XRD)

The structural determination was conducted by using single-crystal X-ray diffraction (SC-XRD). Suitable crystals were coated in *n*-paratone oil, mounted on a Cryoloop, and then transferred onto a goniometer head placed under constant N_2-flux regulated by an Oxford Cryostream cooler system. Intensity data were acquired in ω and φ scans at 100 K employing a Bruker D8 Venture diffractometer equipped with an IμS 3.0 Incoatec microfocus source generating monochromatic Cu K_α radiation (λ = 1.54178 Å) and a Photon III CPAD detector. The data-collection strategy and reduction were performed with the Apex 4 software suite.[53]

The multiscan absorption correction SADABS (2016/2)[54] was performed on all data sets. While the correction substantially improved the internal agreement for **S-Nap_RS-Quin_W** and **S-Nap_SR-Cinch**, the effect on the **S-Ibu_RS-Quin** data set was marginal. Therefore, the structure of **S-Ibu_RS-Quin** was refined using the original uncorrected intensity data.

The structures were solved with the ShelXT structure solution program employing direct methods[55] and refined with the ShelXL[56] refinement package for full matrix least-squares minimization based on F^2 implemented in Olex 2.[57]

The adopted atom labeling scheme, for cations and anions, in all of the structures is reported in Figure S4.

S-Nap_RS-Quin_W. The asymmetric unit comprises a cation−anion pair, consisting of one protonated RS-Quinine molecule and one deprotonated S-Naproxen molecule, in addition to three cocrystallized water molecules, that crystallize in the orthorhombic crystal system, $P2_12_12$ space group. Non-hydrogen atoms were refined anisotropically. Hydrogen atoms of the cation and anion were placed at calculated positions, while H atoms of the water molecules were found in the Fourier maps and modeled by introducing DFIX (0.84 ± 0.01 Å) and DANG (1.33 ± 0.02 Å) commands. The thermal parameters of hydrogen atoms were refined in the riding mode according to the atom to which they bound.

S-Ibu_RS-Quin. The asymmetric unit includes one cation−anion pair composed of a protonated RS-Quinine cation and a S-Ibuprofenate anion crystallizing in the monoclinic crystal system, the $P2_1$ space group. Non-hydrogen atoms were anisotropically refined. Hydrogen atom positions were calculated geometrically, and their thermal parameters were refined using the riding model following their parent atoms. The thermal parameter of C12I was fixed to 0.05 ± 0.02 Å^2 using ISOR restraint.

S-Nap_SR-Cinch. The asymmetric unit contains a cation−anion pair of a protonated SR-Cinchonine cation and a deprotonated S-Naproxenate anion crystallizing into the monoclinic crystal system, the $P2_1$ space group. Non-hydrogen atoms were refined anisotropically. Hydrogen atoms were placed at calculated positions, and their thermal

https://doi.org/10.1021/acs.cgd.5c01538
Cryst. Growth Des. 2026, 26, 955−969

Table 1. Crystal Data, Selected Experimental Details, and Structure Refinement Parameters for S-Nap_RS-Quin_W, S-Ibu_RS-Quin, and S-Nap_SR-Cinch

	S-Nap_RS-Quin_W	S-Ibu_RS-Quin	S-Nap_SR-Cinch
formula moiety	$[(RS\text{-}Quin)^+(S\text{-}Nap)^-]3(H_2O)$	$[(RS\text{-}Quin)^+(S\text{-}Ibu)^-]$	$[(SR\text{-}Chin)^+(S\text{-}Nap)^-]$
empirical formula	$C_{34}H_{38}N_2O_5{\cdot}3(H_2O)$	$C_{33}H_{42}N_2O_4$	$C_{33}H_{36}N_2O_4$
formula weight	608.71	530.68	524.64
temperature, K	100(2)	100(2)	100(2)
radiation type, wavelength (Å)	Cu K_α, 1.54178	Cu K_α, 1.54178	Cu K_α, 1.54178
crystal system	orthorhombic	monoclinic	monoclinic
space group	$P2_12_12_1$	$P2_1$	$P2_1$
cell parameters (Å, °)	a = 6.4194(2)	a = 14.5163(14)	a = 9.5296(3)
	b = 20.1461(5)	b = 6.5007(6), β = 93.528(5)	b = 6.6459(2), β = 98.120(2)
	c = 23.9976(5)	c = 15.3015(14)	c = 22.0827(7)
V (Å^3)	3103.51(14)	1441.2(2)	1384.54(7)
Z	4	2	2
d_{calc} (mg/m^3)	1.303	1.223	1.258
abs coeff (mm^{-1})	0.756	0.632	0.658
crystal size (mm^3)	0.22 × 0.04 × 0.04	0.10 × 0.02 × 0.02	0.18 × 0.02 × 0.02
theta range for data collection	2.86−72.23	2.89−72.53	2.02−68.16
reflections collected	35,028	15,371	15,579
independent reflections	6069 [R(int) = 0.1010]	5419 [R(int) = 0.0878]	4913 [R(int) = 0.0765]
data/restraints/parameters	6069/9/419	5419/7/357	4913/1/355
goodness-of-fit on F^2	1.033	1.094	1.095
Flack parameter	−0.04(14)	0.20(18)	0.0(2)
final R indices [$I > 2\sigma(I)$]	R_1 = 0.0460, wR_2 = 0.0998	R_1 = 0.0662, wR_2 = 0.1719	R_1 = 0.0556, wR_2 = 0.1380
largest diff. peak and hole, e Å^{-3}	0.29 and −0.24	0.57 and −0.35	0.25 and −0.29

parameters were refined using the riding model following their parent atoms.

Table 1 lists the crystallographic data as well as selected experimental parameters and refinement details for **S-Nap_RS-Quin_W**, **S-Ibu_RS-Quin**, and **S-Nap_SR-Cinch** salts. Complete crystallographic data are available at the Cambridge Crystallographic Data Centre under the CCDC identifiers: 2499058, 2499059, and 2499060. The crystallographic representations were generated by using Mercury software (version 2024.3.1).[58]

Powder X-ray Diffraction (PXRD)

Room-temperature powder diffraction data were collected using an Anton Paar XRDynamic 500 diffractometer equipped with the Co $K_{\alpha1}$ radiation (λ = 1.78897 Å) and a Pixos 2000 CdTe detector. The PXRD data were recorded, in Bragg/Brentano geometry, on finely ground samples dispersed on a Si-zero-background sample holder. The scanning covered the angular range of 2θ from 5° to 35°, with a step size of 0.02° and an exposure time of 0.5 s/step.

The same instrument was also used to get the pattern used to obtain the cell parameters of **S-Nap_RS-Quin**. The microcrystalline powder of the anhydrous compound was finely ground and dispersed on a Si zero-background sample holder. The scanning covered the angular range of 2θ (°) from 5° to 35°, with a step size of 0.02° and an exposure time of 0.5 s/step.

For the hydrate salt **R-Nap_RS-Quin_W**, a high-quality PXRD pattern, used to determine its cell parameters, was recorded loading the powder in a 1 mm glass capillary and by using a Bruker New D8 Da Vinci diffractometer (Cu−$K_{\alpha1}$ radiation = 1.54056 Å, 40 kV × 40 mA), equipped with a Bruker LYNXEYE-XE detector. Data were recorded over a 2θ range of 3−40°, with a step size of 0.02° and a counting time of 1.5 s per step (Figure S2b).

Variable temperature (VT-PXRD) measurements were performed on an Anton Paar XRDynamic 500 diffractometer. The **S-Nap_RS-Quin_W** powder sample was placed onto the mid-temperature chamber sample stage of an Anton Paar TTK600. PXRD data were collected while being heated in air from 303 to 433 K in 20 K intervals, at a heating rate of 10 K/min. The diffraction patterns were collected over a 2θ range of 3−35°, using a step size of 0.02° and an exposure time of 80 s per step, following a 5 min stabilization period at each temperature.

The **S-Nap_RS-Quin** and **R-Nap_RS-Quin_W** cell parameters and space group were determined by using EXPO2014;[59] then, the Rietveld method implemented in TOPASv6[60] was used to refine the parameters. Background and peak shapes were fitted using a shifted Chebyshev function with eight coefficients and a Pseudo-Voigt function, respectively.

Differential Scanning Calorimetry (DSC)

Differential Scanning Calorimetry (DSC) experiments were carried out by using a Mettler Toledo DSC1 Excellence instrument. Measurements were run in aluminum pans with pinhole lids (samples' mass ranged from 1 to 3.5 mg). Temperature and enthalpy calibrations were done using indium as the standard. Measurements were carried out in the 303−573 K temperature range, and both linear heating rates of 10 and 2 K/min were used. Experiments were performed in air. DSC peaks were analyzed using the STARe software.[61] The reported data was the average of two measurements with standard errors of ±0.1 K for temperature and ±0.3 kJ/mol for enthalpy.

Thermogravimetric Analysis (TGA)

Thermogravimetric analyses (TGA) on **S-Nap_RS-Quin_W**, **S-Nap_RS-Quin**, and **R-Nap_RS-Quin_W** were performed between 313 and 873 K, under air flow (100 mL/min) and at a heating rate of 10 K/min, with an EXSTAR Thermo Gravimetric Analyzer, Seiko 6200. Data are shown in Supporting Information (Figures S5−S7).

Hot-Stage Microscopy (HSM)

A Leica DM2700 M device connected to a Linkam LTS350 platinum plate was employed to carry out hot-stage characterization on **S-Nap_RS-Quin_W**. Images (shown in Figure S8) were collected with the imaging software Leica Application Suite, from a Leica ICC50 W digital camera.

Cambridge Structural Database Survey

The Cambridge Structural Database version 5.46, update February 2025[51] CSD hereafter, was searched to get insights into the conformational preferences of the propionate moiety, which is common to all the NSAID anions, and of the quinine/cinchonine cations of the

https://doi.org/10.1021/acs.cgd.5c01538
Cryst. Growth Des. 2026, 26, 955−969

Table 2. Crystal Data and Cell Parameters of S-Nap_SR-Quin_W (SC-XRD), R-Nap_SR-Quin_W (PXRD), and S-Nap_SR-Quin (PXRD) at T = 298 K

	S-Nap_SR-Quin_W	R-Nap_SR-Quin_W	S-Nap_SR-Quin
cell parameters (Å,°)	a = 6.5228(15)	a = 6.4777(22)	a = 22.351(3)
	b = 21.201(3)	b = 21.198(8)	b = 6.6019(5), β = 95.979(5)
	c = 23.238(6)	c = 23.260(8)	c = 20.328(2)
V (Å^3)	3213(2)	3193(1)	2983.2(6)
crystal system	orthorhombic	orthorhombic	monoclinic
space group	$P2_12_12_1$	$P2_12_12_1$	$P2_1$
Rwp		11.177	10.648
d_{calc} (mg/cm^3)	1.26	1.27	1.23

salts here presented (Scheme S1 in Supporting Information shows the monitored torsion angles).

In Silico Analysis

The crystal packing of **S-Nap_RS-Quin_W**, **S-Ibu_RS-Quin**, and **S-Nap_SR-Cinch** as well as that of **R-Fbu_RR-Quin**[52] was analyzed with CCDC Mercury (v. 2024.1.0).[58] In order to further investigate the intermolecular interactions that hold together the crystal packing of the salts, Crystal-Explorer25.6 was used.[62] The Hirshfeld surfaces (HS) and their associated 2D fingerprint plots (FPPs) were computed; moreover, pairwise interaction energies between unique closest interacting species were also calculated by using the CE-HF and CE-1p-B3LYP models. In addition, energy frameworks were used to visualize the topology of the intermolecular interactions (neighboring ions/molecules whose atoms fall within 3.8 Å were considered). As for **R-Fbu_RR-Quin**, whose flurbiprofen molecule is affected by disorder, the most populated model was considered in all the calculations.

The analysis of the intercolumn interactions in **S-Ibu_RS-Quin**, **R-Fbu_RR-Quin**, and **S-Nap_SR-Cinch** and, for comparative reasons, in **SR-Quin**[63] and in the naproxen-based salt **S-Nap_S-PEA** ((*S*)-(−)-1-phenylethylammonium(S)-2(6-methoxynaphthalen-2-yl)-propionate))[27] has been done, optimizing the structures at the HSE-3c[64] level of theory using Crystal17[65] software. The level of theory used reproduces the experimental geometries very well, with small differences between the calculated and experimental cell volumes (see Table S3). The largest difference (4.7%) was for **R-Fbu_RR-Quin**, where the structure was solved at room temperature. Intercolumn interactions have been estimated by comparing the total energy of the whole crystal with the energy of a single column. To have a meaningful and normalized quantity to be compared between the different structures, a ppm_E quantity has been defined as the difference in energy between the chain extracted by the structure and the structure, divided by the energy of the structure multiplied per 10^6. The energy of the chain is calculated without reoptimizing the structure. The single point calculation was performed as a 1D system (POLYMER keywords in Crystal17), exploiting the fact that in the systems considered, the chains are parallel to a crystallographic axis. The results are reported in Table S4.

Hydration and Dehydration Tests

The potential transformations between anhydrous and hydrated phases were investigated by using different approaches. To assess the hydration tendency, the anhydrous **S-Ibu_RS-Quin** salt (as well as the anhydrous phase obtained by heating **S-Nap_RS-Quin_W** and **R-Nap_RS-Quin_W**; see Discussion) was placed in a desiccator, at room temperature, with a constant relative humidity of approximately 75% (using a saturated NaCl solution) for a period of 10 days. As an alternative procedure, the anhydrous salt was ground for 1 min with a drop of water. To evaluate the dehydration propensity of **S-Nap_RS-Quin_W** and **R-Nap_RS-Quin_W**, the salts were stored in a desiccator with P_2O_5 for 10 days.

In all cases, the resulting powders were analyzed by PXRD.

Preliminary Selective Crystallization Test

RS-quinine was added in the amount of 0.5 mmol to an equimolar ethanolic (8 mL) solution of S-Naproxen (0.5 mmol) and R-Naproxen (0.5 mmol). After the addition of 3 mL of deionized water, the instantly formed precipitate was collected by filtration. The PXRD of the resulting powder sample (SCT_sample) was collected and compared to the simulated PXRD data of **S-Nap_RS-Quin_W**, the experimental PXRD patterns (collected at rt) of **S-Nap_RS-Quin_W**, **R-Nap_RS-Quin_W**, and with those of the starting reagents. Moreover, an analysis by FTIR in ATR mode and the measurement of the optical rotation value was conducted on the same samples (vide infra). Finally, optical rotation measurements were performed on a JASCO DIP-370 polarimeter.

Fourier Transform Infrared Spectroscopy in Attenuated Total Reflection mode (FTIR-ATR)

Analysis by Fourier Transform Infrared Spectroscopy (FTIR) in Attenuated Total Reflection mode (ATR) was performed on an IRAffinity-1S by SHIMADZU, equipped with the ATR sampling accessory (MIRacle PIKE Technologies)[66] and a ZnSe crystal element. Spectra were collected in the 4000−600 cm^{-1} range, with 12 scans for each measurement. Along with the powder sample obtained from the selective crystallization test (SCT_sample), the spectra of **S-Nap_RS-Quin_W**, **R-Nap_RS-Quin_W**, and the reagents were also collected for comparison. Details are provided in Supporting Information.

RESULTS

Salts Synthesis

Samples of **S-Nap_RS-Quin_W** and **S-Ibu_RS-Quin** were successfully synthesized in both single-crystal and microcrystalline powder forms (see Figures S1 and S3). High-quality single crystals, suitable for SCXRD analysis, were obtained via slow solvent evaporation over 2 to 7 days, respectively, while the microcrystalline powder formed instantly by precipitation from EtOH/water solution. In contrast, **S-Nap_SR-Cinch** was obtained exclusively as single crystals. Efforts to obtain microcrystalline **S-Nap_SR-Cinch** using various solvents or their mixtures (see Table S2), both at room temperature and under heating conditions, were unsuccessful as no formation of solid material was observed.

Additional crystallization attempts aimed at obtaining the anhydrous phase of the (S)-Naproxen RS-Quinine salt, using solvents such as acetonitrile and tetrahydrofuran (with water present only as a trace impurity), were unsuccessful. In all cases, crystallization resulted in the formation of the hydrate **S-Nap_RS-Quin_W** (see Figure S9), which definitely appears to be the preferred species.

Moreover, crystallization of R-Naproxen with RS-Quinine resulted in the formation of a novel microcrystalline phase (no single crystals were obtained; see Table S1), named **R-Nap_RS-Quin_W**. Unit cell dimensions were determined by indexing the high-quality PXRD, and parameters are reported in Table 2.

Molecular Structures from Single-Crystal X-ray Diffraction

The asymmetric unit of the **S-Nap_RS-Quin_W**, **S-Ibu_RS-Quin**, and **S-Nap_SR-Cinch** salts contains one NSAID anion

https://doi.org/10.1021/acs.cgd.5c01538
Cryst. Growth Des. 2026, 26, 955−969

and one *Cinchona* alkaloid cation; in addition, **S-Nap_RS-Quin_W** also includes three water molecules (Figure 1). For comparative purposes, the structure of **R-Fbu_RR-Quin** (CCDC refcode: **IGATOC**)[52] was also included in the following discussion. As for the anions, in all cases, the orientation, with respect to the aromatic ring, adopted by the propionate moiety is quite similar (Figure S10a) and falls into the more populous region, as provided by a search performed in the CSD for the fragment sketched in Scheme S1. As expected, the RS-Quin cations in **S-Ibu_RS-Quin** and **S-Nap_RS-Quin_W** are almost perfectly superimposable (Figure S10b). More in general, the monitored torsion angles (Scheme S1) agree well with those that characterize the quinine/cinchonine cations having the same stereochemistry at all the stereocenters.

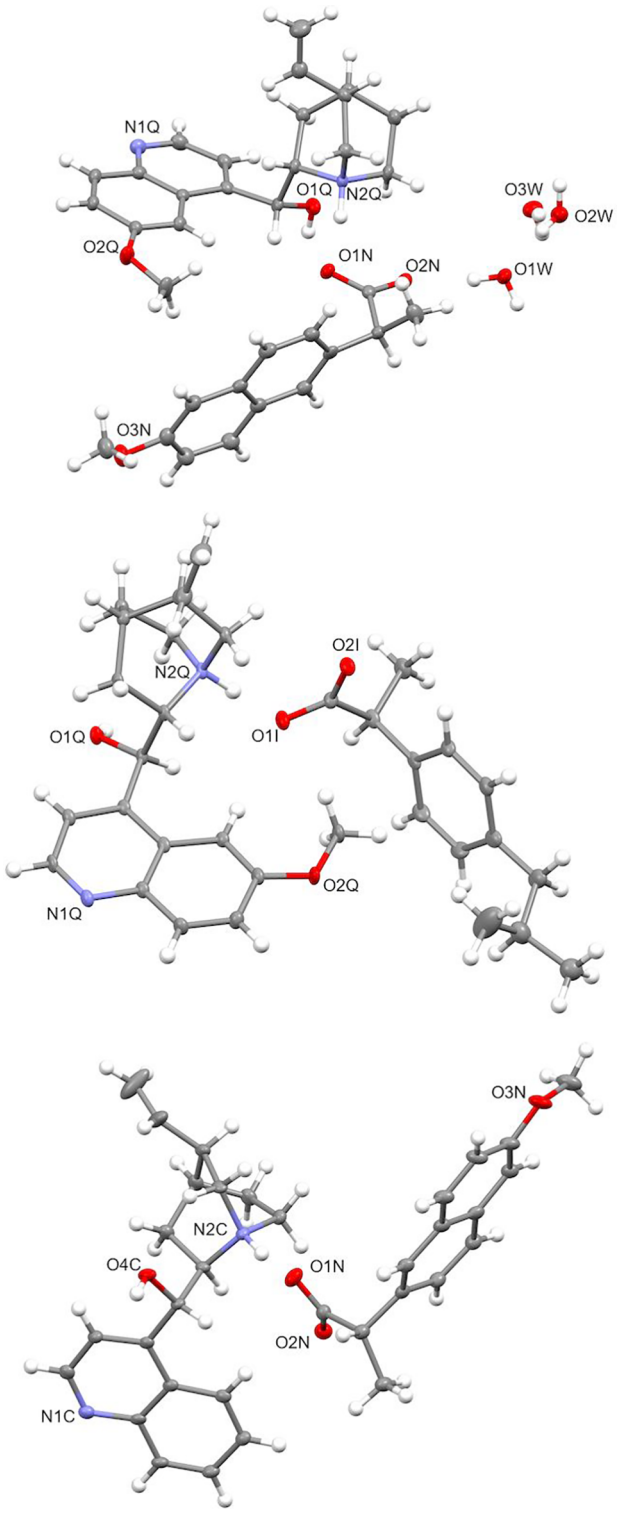

Figure 1. ORTEP-3 view of the asymmetric units (from top to bottom) of **S-Nap_RS-Quin_W**, **S-Ibu_RS-Quin**, and **S-Nap_SR-Cinch** showing the oxygen and nitrogen labels. Thermal ellipsoids are drawn at the 30% probability level). The atom labeling scheme adopted for all the structures is reported in Supporting Information.

Crystal Structures from Single-Crystal X-ray Diffraction and In Silico Methods

Despite the varied nature of the components, including the specific NSAID used (ibuprofen, naproxen, or flurbiprofen) and its absolute configuration (S or R), the specific alkaloid (quinine or cinchonine) and its stereochemistry (RS, SR, or RR), and the possible presence of cocrystallized water (as in **S-Nap_RS-Quin_W**), in all the crystal structures, hydrogen-bonded anions and cations (each related by translational symmetry) are arranged in columns, which extend along the shortest crystallographic axis direction. However, while the overall motif (the column) is maintained across all structures, a difference in the reciprocal arrangement of the cation−anion pair is observed: the quinoline ring of the alkaloid is face-to-face with the aryl portion of the NSAID skeleton in the S-anion-RS-cation and R-anion-RR-cation pairs; conversely, they are oriented on opposite sides in the case of the S-anion-SR-cation combination. This difference (face-to-face versus opposite arrangement) suggests a possible chiral influence in driving the relative orientation of the paired ions.

In all of the salts, the NSAID and quinine/cinchonine ions are assembled through the ammonium-carboxylate ($NH^+\cdots{}^-OOC$) and hydroxyl-carboxylate ($OH\cdots{}^-OOC$) supramolecular heterosynthons, which are also observed in the hydrated species **S-Nap_RS-Quin_W**. The resulting H-bond motif (Figure 2) can be categorized as $C_2^2(9)$ according to the graph set notation,[67] and it is quite usual in crystal structures comprising the carboxylate anion and the fragment sketched in Scheme S1, as evidenced by a search performed in the CSD.[68]

On the basis of the donor···acceptor distances defining the $NH^+\cdots{}^-OOC$ and $OH\cdots{}^-OOC$ hydrogen bonds, which are comprised between 2.550(5) and 2.691(3) Å and 2.652(4) and 2.703(4) Å, respectively (see Tables S5−S7), they can be classified as strong.[69] In the strictly related structure **R-Fbu_RR-Quin** also the $NH^+\cdots{}^-OOC$ and $OH\cdots{}^-OOC$ bonds are strong (both D···A distances are 2.53 Å).

Consistently, the Hirshfeld surfaces (HSs) of the NSAID anions are characterized by 2 large red spots related to the strongest H-bonds involving the already mentioned heterosynthons (Figures S11 and S12). Moreover, in **S-Nap_RS-Quin_W**, a further well-evident red spot is present nearby the carboxylate oxygen atom involved in the $NH^+\cdots{}^-OOC$ interaction, highlighting a strong H-bond with a water molecule (O1W−H1WA···O2N, 2.736(3) Å). Less pronounced red spots are also present which, for example, evidence that the carboxylate oxygen atom involved in the $OH\cdots{}^-OOC$ hydrogen bond also acts as a weak acceptor toward the CH group provided by a close quinine cation as in **S-Ibu_RS-Quin** (C17Q-H17A···O2I, 3.379(5) Å), in **S-Nap_RS-Quin_W** (C10Q-H10B···O1N, 3.251(5) Å), or in **S-Nap_SR-Cinch** (C9C−H9C···O2N, 3.393(5) Å). Moreover, in the naproxen-based salts, red pale regions signal that also the oxygen atom of the methoxy group is

https://doi.org/10.1021/acs.cgd.5c01538
Cryst. Growth Des. 2026, 26, 955−969

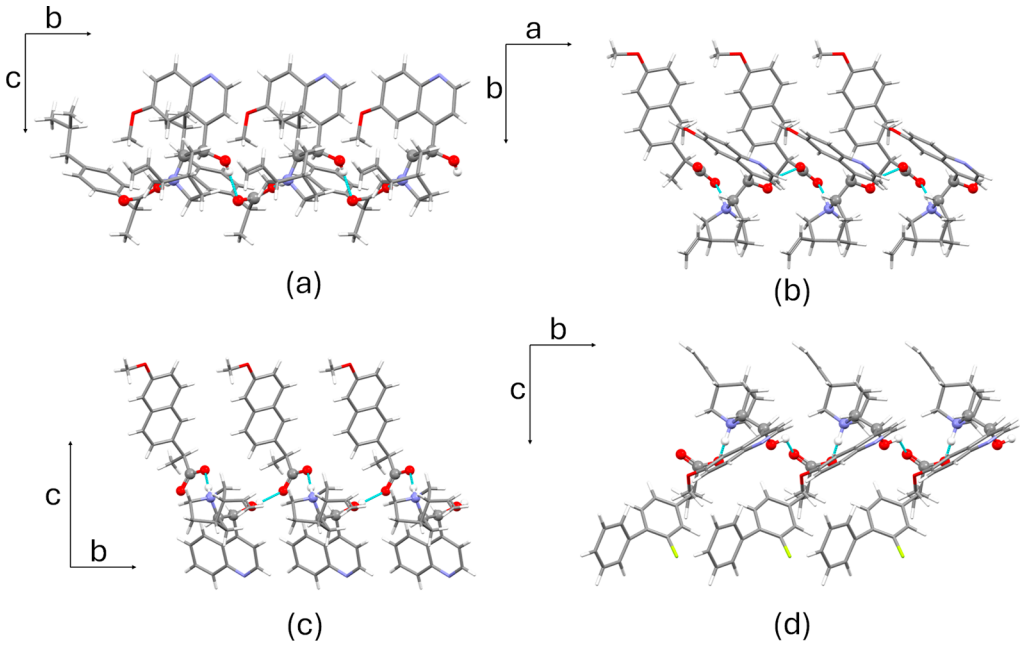

Figure 2. Ionic pairs extending along the shortest axis direction, which originate columns in (a) **S-Ibu_RS-Quin** viewed along a; (b) **S-Nap_RS-Quin_W** viewed along b; (c) **S-Nap_SR-Cinch** viewed along a; and (d) **R-Fbu_RR-Quin** viewed along a.

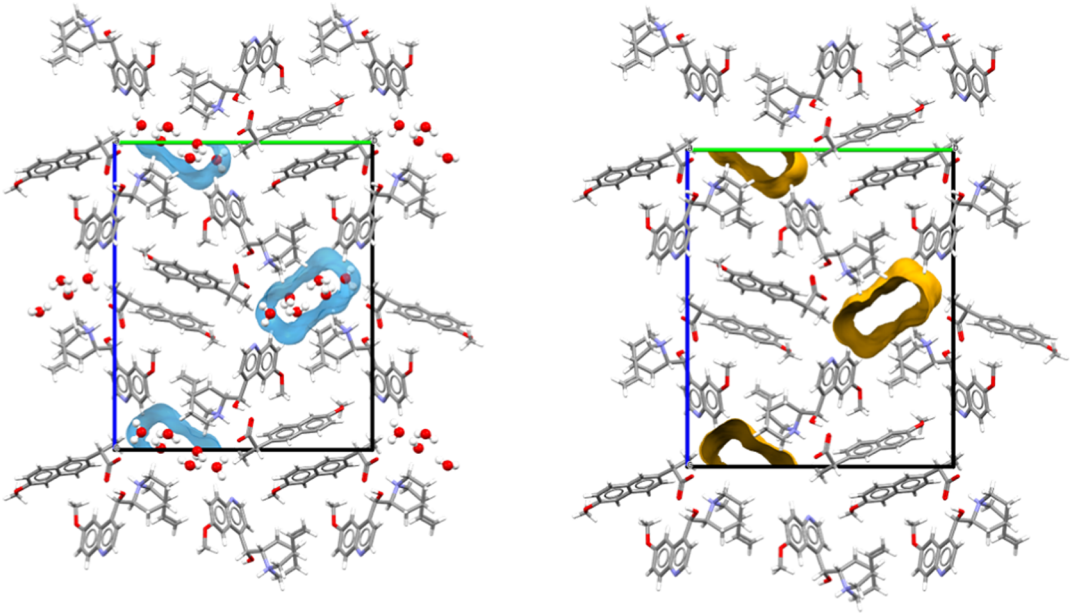

Figure 3. Crystal packing of **S-Nap_RS_Quin_W**: view along the *a*-axis direction highlighting the water molecules hosted within the channel (left) and the void space resulting from their in-silico removal (right).

involved in several interactions (in **S-Nap_RS-Quin_W**: C3Q-H3Q···O3N, 3.290(4) Å; in **S-Nap_SR-Cinch**: C18C−H18A···O4C, 3.270(5) Å and C16C−H16A···O3N, 3.403(5) Å. In **R-Fbu_RR-Quin**, a quite pronounced red spot evidence a CH···π interaction involving the quinine methoxy and the flurbiprofen phenyl ring (CH···centroid, 2.38 Å).

As for the RS-Quin/SR-Cinch cations, in addition to the well evident red spots related to the ammonium and hydroxyl H-bond donors, a third one in **S-Nap_RS-Quin_W** should be mentioned, which well highlights the involvement of the pyridine moiety as the H-bond acceptor (O1W−H1WB···N1Q, 2.844(4) Å, Table S6). Less visible red spots also evidence that the oxygen atom of the hydroxyl group acts also as a weak H-bond acceptor toward the CH provided by a symmetry-related cation as in **S-Ibu_RS-Quin** (C16Q-H16B···O1Q, 3.085(5) Å) and in **S-Nap_RS-Quin_W** (C16Q-H16B···O1Q, 3.369(4) Å).

Pair-wise intermolecular interaction energies indicate that, as a whole, the ionic pair held together by the $NH^{+}\cdots{}^{-}OOC$ bond is definitely more stabilized with respect to that bound through the $OH\cdots{}^{-}OOC$ bond; in fact, differences between pairwise intermolecular interaction energies (CE-1p-B3LYP model) range from about 195 kJ/mol in the naproxen-based salts to 126 kJ/mol in the ibuprofen- and flurbiprofen-based ones.

In the hydrated species **S-Nap_RS-Quin_W**, the three water molecules are located in channels extending along the shortest

https://doi.org/10.1021/acs.cgd.5c01538
Cryst. Growth Des. 2026, 26, 955−969

axis direction (Figure 3). The space occupied by the water molecules, calculated using the contact surface with the Hydrate Analyzer tool of Mercury (probe radius 1.2 Å, approximate grid spacing 0.3 Å) is about 10% of the unit cell volume.

Interestingly, the three molecules experience different environments, as evidenced by the related HSs: four well-evident red spots for the water molecules O1W and three for O2W and O3W. In particular, O1W works as an intercolumn bridge acting as the H-bond donor toward the carboxylate oxygen atom, O2N (O1W−H1WA···O2N, 2.736(3) Å) and the pyridine nitrogen atom, N1Q (O1W−H1WB···N1Q, 2.844(4) Å) belonging to adjacent columns. In addition, it works as a bifurcated acceptor toward the O2W and the O3W (O2W−H2WA···O1W, 2.813(4) Å and O3W−H3WB···O1W 2.862(4) Å, respectively): these latter further act as H-bond acceptor (O2W−H2WB···O3W, 2.757(4) Å) and donor (O3W−H3WA···O2W, 2.741(4) Å) toward each other. The pairwise intermolecular interaction energies involving the water molecules are almost the same including the O1W···N1Q H-bonding interaction (about −19 kJ/mol, CE-1p-B3LYP model), except for the OW1−H···$^{-}$OOC which, as expected, is definitely more stabilizing (O1W−H1WA···O2N, 2.736(3) Å, −50.2 kJ/mol, CE-1p-B3LYP model).

As a whole, the self-assembly of the cocrystallized water molecules describes a $R_5^4(10)$ motif according to the graph set notation (Figure 4).

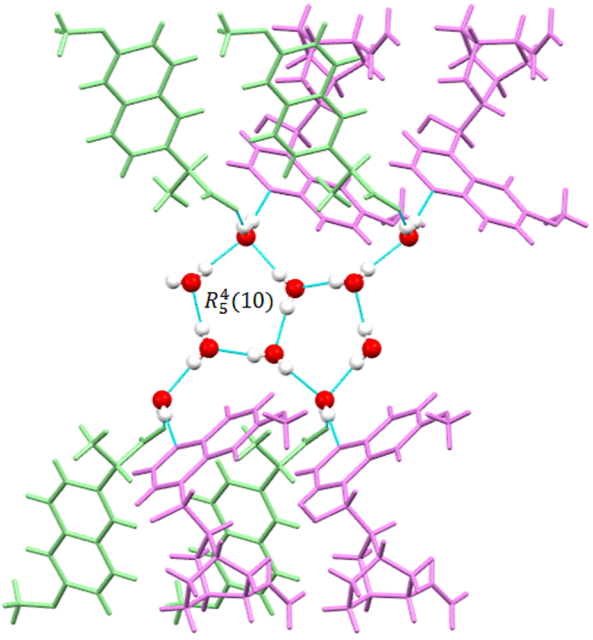

Figure 4. S-Nap_RS-Quin_W: view of the hydrogen bond network involving the cocrystallized water molecules along the *c* axis.

Based on the Morris classification,[70−72] the hydrate can be classified as a channel hydrate (the water molecules, which are H-bonded but also are involved in interactions with the host species, are close each other and form channels or layers along a given crystallographic direction).

Figures S13−S19 show the related fingerprint plots. The O(in)···H(out) contribution to the HSs is definitely bigger for the (S)-naproxen anions (17.9% in **S-Nap_SR-Cinch** and **S-Nap_RS-Quin_W**, respectively vs 12.2% and 13.2% in **R-Fbu_RR-Quin** and **S-Ibu_RS-Quin**, respectively) and well evidence the contribution of the methoxy oxygen atom to the crystal packing. As for the quinine cations, the bigger contribution related to the H(in)···O(out) interactions, which characterizes the **S-Nap_RS-Quin_W** salt with respect to the other ones containing the quinine cation (13.0% vs about 8% in **S-Ibu_RS-Quin** and **R-Fbu_RR-Quin**, respectively), reflects the presence of weak CH···O interactions involving the cocrystallized water molecules O2W and O3W.

As for the O1W, its involvement as the H-bonds donor toward the carboxylate oxygen atom and the pyridine nitrogen atom accounts for 26% of the related HS (H(in)···O(out), 13.0 e H(in)···N(out) 13.1%) vs 21.7 and 18.3% for the O2W and the O3W, respectively.

Energy frameworks were then used to obtain a graphical and quantitative representation of the topological arrangement and relative strengths of the intermolecular interaction energies within each salt. Figures 5 and 6 clearly illustrate the layered

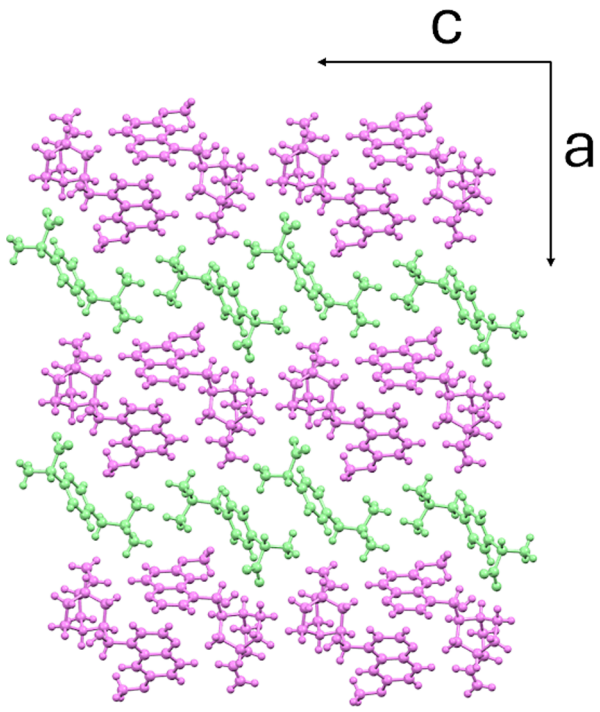

Figure 5. Crystal packing of **S-Ibu_RS-Quin** showing the layered architecture made of alternating anionic (green) and cationic (pink) species.

architecture made of alternating anionic (green) and cationic (pink) species piling along the a- and *c*-axis direction in **S-Ibu_RS-Quin** and **R-Fbu_RR-Quin**, respectively. As expected, the interactions are predominantly Coulomb-based, as clearly shown by the energy-framework diagrams (see Figures S20 and S21), where the magnitude of the Coulomb energies closely mirrors the total energies (the energy components for the more important pairwise interactions are reported in Table S8). As already pointed out, the most significant stabilizing interactions occur between cation−anion pairs situated within each column (which extends along the *b*-axis direction) and provided by contiguous layers. As a whole, intercolumn interactions appear less significant. A layered structure is also observed in **S-Nap_SR-Cinch**, repeated along the *c*-axis direction. In this case, however, the relative arrangement of the cations (pink) originates a sort of bilayer, as well-illustrated in Figure 7. In

https://doi.org/10.1021/acs.cgd.5c01538
Cryst. Growth Des. 2026, 26, 955−969

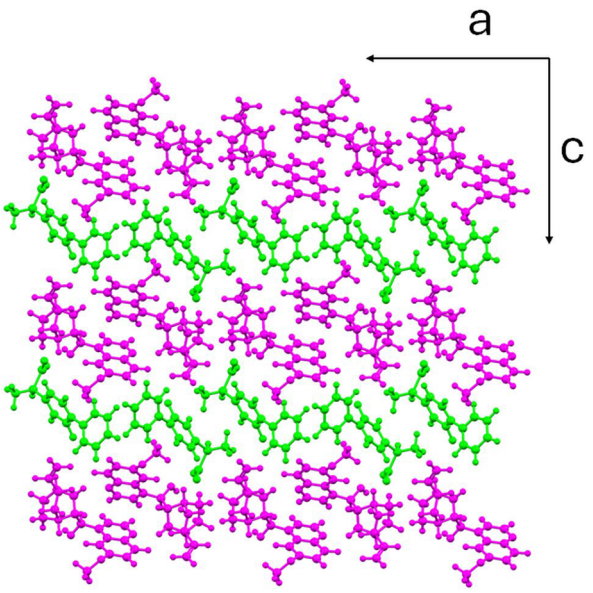

Figure 6. Crystal packing of **R-Fbu_RR-Quin** showing the layered architecture made of alternating anionic (green) and cationic (pink) species.

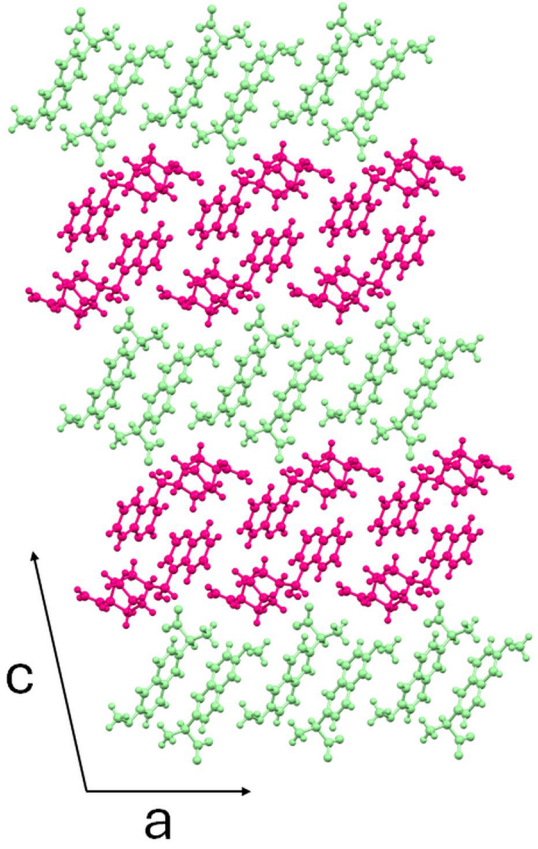

Figure 7. Crystal packing of **S-Nap_SR-Cinch** showing the bilayer originating from the relative arrangement of the cations (pink).

this case also, the strongest stabilizing interaction (mostly Coulomb-based; see diagrams in Figure S22 and Table S8) involves cation−anion pairs located within each column and belonging to adjacent layers. The energy framework diagram for E_{tot} reveals definitely a more anisotropic distribution of the intermolecular interactions with respect to the above-discussed quinine-based structures (i.e., cation vs anion layer); moreover, the interactions involving the cations within the bilayer are destabilizing, thus suggesting a potential propensity for cleavage parallel to the *a*-axis direction.

The columnar arrangement observed in the three anhydrous structures described above is also observed in the crystal structures of **SR-Quin**[64] and **SR-Cinch**[73] (columns are made of OH···N bonded cinchona alkaloid molecules). Interestingly, a similar arrangement was reported for the acid *S*-Naproxen (while in the acid naproxen racemate as well as in the acid ibuprofen racemate and single enantiomer, dimers are observed). As expected, the salts energy framework diagrams confirm that the strongest interactions occur within the columns, the intercolumn interactions being definitively negligible.

By using Crystal 17 (details in the Experimental Section), the intercolumn interactions in the three anhydrous salts as well as in quinine (**SR-Quin**) have been analyzed by comparing the total energy of the whole crystal with the energy of a single column. Additionally, for comparative reasons, the naproxen-based salt **S-Nap_S-PEA**[27] ((*S*)-(−)-1-phenylethylammonium ((*S*)-2-(6-methoxynaphthalen-2-yl) propionate)), also featuring a column of tightly interacting ions via $NH^{+}\cdots{}^{-}OOC$ bonds and less significant intercolumn interactions, was considered. The estimated energy for the intercolumn interactions is reported in Table S4. All of the calculated values for quinine and the four organic salts are in the same range. On this basis, we can speculate that the contribution of the intercolumn interactions to the overall crystal stability is definitely only slightly influenced by the nature of the column constituents.

In the case of **S-Nap_RS-Quin_W**, the alternating cation−anion layers stack along the *c*-axis direction, with anions arranged in pairs and separated by intercalated water molecules (Figure S23). In contrast to the previously discussed quinoline-based salts, these layers exhibit a wavy morphology.

Nonetheless, a recurrent topological arrangement of intermolecular interaction energies emerges across all quinine-containing salts, regardless of the nature and stereochemistry of the NSAID, the stereochemistry of quinine itself, or the presence of cocrystallized water (as shown in Figures S20, S21, and S23, bottom).

Variable Temperature Analysis

Thermogravimetric analysis (TGA) and differential scanning calorimetry (DSC) experiments were performed to assess the thermal stability of all synthesized samples. The TGA data of **S-Nap_RS-Quin_W** (Figure S5) indicates a weight loss of about 8.0% at 373 K. This value is compared with the theoretical weight loss of 8.9% calculated for the loss of three molecules of lattice water, as determined by the SC-XRD analysis. The DSC curve (Figure S5) shows, within the temperature range of 303−573 K, two endothermic and one exothermic event. The first endothermic peak, occurring at 362 K (peak = 362.1 K and extrapolated peak = 363 K, enthalpy = 144.6 kJ/mol), was attributed to the loss of water and the concomitant melting (vide infra), while the exothermic peak at 401 K (peak = 400.7 K, extrapolated peak = 400.8 K, enthalpy = −15.8 kJ/mol) was attributed to the recrystallization of a new phase, which subsequently melted at 430 K (peak = 430.2 K and extrapolated peak = 430.6 K, enthalpy = 43.9 (kJ/mol). Melting and subsequent recrystallization were also observed during the hot-stage microscopy (HSM) experiment, with a noticeable shift in the temperatures at which these transitions occurred. This

https://doi.org/10.1021/acs.cgd.5c01538
Cryst. Growth Des. 2026, 26, 955−969

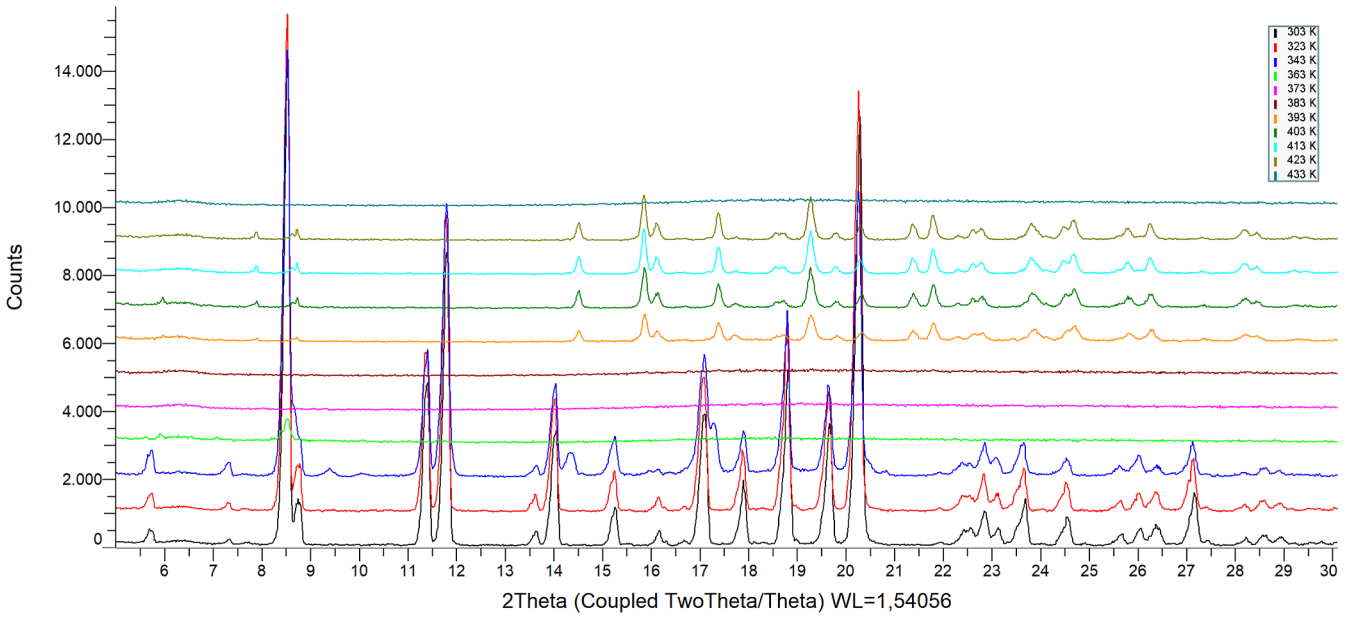

Figure 8. Variable-temperature PXRD patterns of **S-Nap_RS-Quin_W** collected from 303 to 433 K, showing an initial melting event starting at 363 K, followed by recrystallization into a new crystalline phase at 393 K, which undergoes complete melting at 433 K.

variation is likely due to differences in the experimental setup and the physical form of the starting material (single crystal vs microcrystalline powder). Specifically, melting began at approximately 393 K, while recrystallization was observed around 473 K (Figure S8).

To gain deeper insight into the thermal behavior of **S-Nap_RS-Quin_W** and to better identify the phases arising from the thermal events observed in the DSC experiments, we performed in situ variable-temperature powder X-ray diffraction (VT-PXRD) analysis. Powder diffraction patterns (Figure 8) were recorded within approximately the same temperature range as the DSC analysis, revealing consistent results between the two techniques. Notably, at 363 K, no crystalline peaks were detected, confirming that the solid had melted. At 393 K, the appearance of a new diffraction pattern was observed, revealing the formation of a new crystalline phase. Finally, the PXRD pattern acquired at 433 K confirmed the melting of this newly formed phase, as no diffraction peaks were present, consistent with the DSC findings. The microcrystalline powder **S-Nap_RS-Quin_W** was also thermally treated at 433 K in an oven for 1 h to induce dehydration, melting, and subsequent recrystallization. Consistent with previous observations, the resulting phase exhibited a PXRD pattern comparable to that recorded at 413 K during the in situ VT-PXRD experiment. This new solid form was designated as anhydrous **S-Nap_RS-Quin**, based on the TGA curve (see Figure S6). Indexing of the powder diffraction pattern enabled the determination of the unit cell parameters, crystal system, and space group of this anhydrous phase (see Table 2 and Figure S24). Unfortunately, although several attempts were made, it was not possible to obtain a PXRD pattern good enough to allow the resolution of the structure of this anhydrous phase.

For the structurally unknown diastereoisomeric salt **R-Nap_RS-Quin_W**, DSC analysis (Figure S7) revealed a single endothermic event, indicating melting at 348 K (peak = 348.1 K, extrapolated onset = 350.5 K, and enthalpy = 208.4 kJ·mol^{-1}). The broad nature of this peak suggested a concurrent loss of water, which was confirmed by TGA analysis. In fact, at the same temperature (347 K), a weight loss of about 8% (comparable with the presence of 3 crystallization water molecules (theoretical weight loss for 3 water molecules = 8.9%)) was observed (see Figure S7).

Finally, the DSC analysis of **S-Ibu_RS-Quin** (Figure S25) revealed a single endothermic event at 426 K (peak = 426.4 K, extrapolated peak = 426.2 °C, and enthalpy = 53.4 kJmol^{-1}), corresponding to the melting of the solid phase.

Hydration and Dehydration Tests

To assess the stability of the hydrated phases of the naproxen/RS-quinine salts (**S-Nap_RS-Quin_W** and **R-Nap_RS-Quin_W**) with respect to dehydration, their powder samples were placed in a sealed chamber containing the strong dehydrating agent P_2O_5. After 10 days, PXRD analysis of the **S-Nap_RS-Quin_W** sample revealed the appearance of the anhydrous form **S-Nap_RS-Quin**, previously identified by in situ VT-PXRD and ex situ PXRD (Figure S26). Rehydration was observed upon placing a sample of **S-Nap_RS-Quin** in a closed chamber at approximately 75% relative humidity for 1 week, as evidenced by the emergence of diffraction peaks corresponding to the **S-Nap_RS-Quin_W** phase (Figure S26).

Different was the behavior of the salt **R-Nap_RS-Quin_W**. In fact, this hydrated phase did not lose crystallization water molecules in the same investigated condition (put in a sealed chamber with P_2O_5 for 10 days), remaining stable (Figure S27). Finally, the anhydrous sample, obtained by heating **R-Nap_RS-Quin_W** powder in an oven at 353 K, was stable if placed in a closed chamber at approximately 75% relative humidity for 1 week but gave the hydrated species **R-Nap_RS-Quin_W** if ground with two drops of water (see Figure S27).

Finally, hydration tests on the anhydrous **S-Ibu_RS-Quin** were conducted following the previously described procedure (the sample was maintained at a constant relative humidity of approximately 75% for 2 weeks). At the end of the experiment, the PXRD analysis showed no detectable changes, indicating the stability of the phase under these conditions. Similarly, grinding the **S-Ibu_RS-Quin** powder in the presence of two drops of

https://doi.org/10.1021/acs.cgd.5c01538
Cryst. Growth Des. 2026, 26, 955−969

Scheme 2. Schematic Representation of the Hydration and Dehydration Procedures and Observed Stability/Conversion Pathways for the S-Ibu_RS-Quin and Naproxen/RS-Quinine Salts (S-Nap_RS-Quin_W and R-Nap_RS-Quin_W)

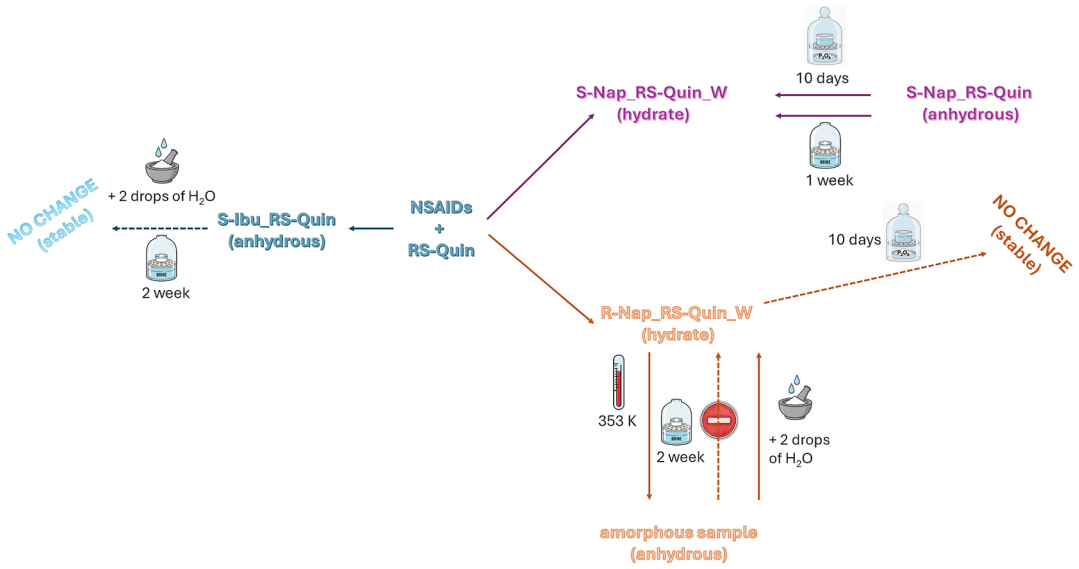

water produced no observable transformations, further confirming its resistance to hydration (Figure S28).

A schematic panel of the different dehydration and hydration procedures is reported in Scheme 2.

Preliminary Selective Crystallization Test

A preliminary selective crystallization experiment was conducted to assess the potential of RS-quinine as a resolving agent for racemic naproxen. The procedure employed was based on Markwald's method,[4,74] which involves the addition of a half-equivalent of the resolving agent to a racemic solution, thereby promoting the selective crystallization of one enantiomer while the other remains in the mother liquor or forms a separate phase. Water and ethanol were used as solvents, and the crystallization protocol mirrored that employed for the synthesis of the microcrystalline powders **S-Nap_RS-Quin_W** and **R-Nap_RS-Quin_W** (see Experimental Section for details). The resulting solid (SCT_sample) was characterized by PXRD (Figure S29), IR spectroscopy (SI), and polarimetry (see Supporting Information). These analyses consistently indicated that the sample contains exclusively the **S-Nap_RS-Quin_W** diastereomeric salt (no evidence of the presence of **R-Nap_RS-Quin_W** was found), along with approximately 20% of naproxen acid as an impurity.

To facilitate the subsequent discussion, the key findings regarding the structural relationships and hydration behavior of the analyzed salts are synthesized below:

- Across all analyzed structures, a consistent motif emerges: the formation of H-bonded anion−cation columns parallel to the shortest crystallographic axis. Energy framework analysis reveals a distinct intermolecular interaction topology in the cinchonine-based salt compared to the quinine salts. For the latter, the primary interaction motif is essentially preserved, irrespective of the NSAID nature, its stereochemistry, or the quinine stereochemistry.
- In **S-Nap_RS-Quin_W**, water molecules occupy channels parallel to the columns and contribute only marginally to crystal packing stabilization. This salt undergoes simultaneous dehydration and melting, followed by recrystallization into the anhydrous **S-Nap_RS-Quin** form, losing water even under P_2O_5. The process is reversible, as controlled humidity restores the hydrated phase. The hydrated and anhydrous forms show similar cell parameters, although the anhydrous phase displays lower symmetry.
- The two hydrated diastereomeric salts (**S-Nap_RS-Quin_W** and **S-Nap_RS-Quin_W**) have very similar unit cells. **R-Nap_RS-Quin_W** dehydrates and melts without recrystallizing. The anhydrous R-Nap/RS-Quin does not rehydrate at 75% RH, but the hydrated phase reforms upon grinding with water. Notably, **R-Nap_RS-Quin_W** remains stable in a sealed chamber with P_2O_5 for 10 days.
- The anhydrous **S-Ibu_RS-Quin** phase remains stable at ∼75% relative humidity for 2 weeks and shows no transformation upon grinding in the presence of water.
- Preliminary selective crystallization experiments suggest a preferential association of RS-Quin with the *S*-enantiomer of naproxen.

DISCUSSION

Although it was not possible to determine the solid-state crystal structures of **R-Nap_SR-Quin_W** and **S-Nap_SR-Quin**, several inferences can be made regarding the packing of the cation and anion within these crystal structures.

First, a comparative analysis of the salts **S-Nap_RS-Quin_W**, **S-Nap_SR-Cinch**, **S-Ibu_RS-Quin**, and **R-Ibu_RR-Quin** reveals the ubiquitous presence of a strong supramolecular synthon that binds the nonsteroidal anti-inflammatory drug (NSAID) and the alkaloid ions. This synthon is consistently responsible for generating columns formed by alternating hydrogen-bonded anions and cations. These columns extend along the shortest crystallographic axis via translational symmetry.

Crucially, this packing arrangement persists regardless of the specific NSAID cation, the enantiomer selected, the chirality of the alkaloid, or the presence or absence of crystallization water. As for these latter in the hydrated salt **S-Nap_RS-Quin_W**, only

https://doi.org/10.1021/acs.cgd.5c01538
Cryst. Growth Des. 2026, 26, 955−969

one of the three cocrystallized water molecules is directly involved in bridging the two chiral ions, acting as a structural link between columns. Moreover, this interaction is, as expected, decidedly weak (based on calculated pairwise interaction energies); then we can speculate that water does not play an essential role in the fundamental chiral recognition event.

Considering this stable and recurring columnar structure, it is reasonable to hypothesize that a similar H-bond motif exists between the cation and anion in the **S-Nap_SR-Quin** and **R-Nap_SR-Quin_W** salts.

Furthermore, in the case of **S-Nap_RS-Quin_W**, the water molecules are situated within channels that run parallel to the *a*-axis and exhibit a two-dimensional ordered arrangement. These water molecules participate in hydrogen bonding both with the host lattice and with each other. Specifically, one water molecule is bound to the host framework via robust hydrogen bonds, while the remaining two are more loosely associated and primarily engage in self-interaction. Based on these structural characteristics, this phase is correctly classified as a channel hydrate, accordingly to Morris and Vippagunta[70−72] who classified crystalline hydrates into three categories based on the location and role of the water molecules: isolated site hydrates, channel hydrates, and ion-associated hydrates.

Concerning the anhydrous phase **S-Nap_RS-Quin**, the observed reversibility of the dehydration−hydration processes provides important hints. This phase, which is the result of the dehydration process of **S-Nap_RS-Quin_W** when stored with P_2O_5, is stable under ambient conditions for at least 10 days and can be rehydrated at 75% relative humidity. This reversibility, coupled with the similar cell parameters found in the two compounds, suggests the persistence of channels, even in the anhydrous phase.

On the other hand, the **R-Nap_RS-Quin_W** salt presents a different scenario compared to **S-Nap_RS-Quin_W**.

First, infrared analysis (SI) suggests that the coordination mode of the crystallization water molecules in the R-Nap/RS-Quin hydrate salt is different from that in **S-Nap_RS-Quin_W**, with the latter exhibiting stronger water bonding.

Second, differential scanning calorimetry and variable temperature X-ray powder diffraction analyses confirm a significant difference in their stability:

1. Dehydration outcome: heating **R-Nap_RS-Quin_W** leads to the loss of water molecules and the formation of an amorphous phase, whereas the dehydration of **S-Nap_RS-Quin_W** results in a stable anhydrous crystalline phase.

2. Rehydration irreversibility: the amorphous phase obtained from the dehydration of **R-Nap_RS-Quin_W** cannot be rehydrated simply by exposure to 75% relative humidity (in contrast to its diastereomeric salt). Rehydration in this case requires grinding with a few drops of water.

3. Hydrate stability: the salt **R-Nap_RS-Quin_W** remained stable after 10 days of exposure to P_2O_5 differently from **S-Nap_RS-Quin_W**, which in the same conditions loses its water molecules (forming **S-Nap_RS-Quin**).

Although the cell parameters of the two hydrated salts are similar (see Table 2), the differences in their diffraction profiles suggest that their crystal packing is not identical, a feature previously observed in other diastereomeric salts.[75−77] This may be due to a different relative arrangement of the columnar units as well as of the crystallization water molecules within the crystal lattice.

These differences in the thermal and structural stabilities observed in the hydrated diastereomeric salts likely play a crucial role in the selective crystallization outcomes, thus proving the importance of a systematic study of solid-state forms to move beyond the time-consuming trial-and-error approach in the selection of resolving agents.

CONCLUSIONS

The comparative structural analysis across four different salts (**S-Nap_RS-Quin_W**, **S-Nap_SR-Cinch**, **S-Ibu_RS-Quin**, and **R-Fbu_RR-Quin**), reported in the present article, consistently demonstrated the presence of a strong supramolecular synthon that establishes columns of alternating hydrogen-bonded anions and cations along the shortest crystallographic axis. Actually, this columnar packing motif is highly robust, maintaining its organization regardless of the specific components or the inclusion of crystallization water. On this basis, the presence of an analogous cation−anion columnar motif can be confidently hypothesized in the crystal structures of the **S-Nap_SR-Quin** and **R-Nap_SR-Quin_W** salts.

However, the two naproxen/RS-quinine diastereomeric hydrates exhibit different structural and thermal stabilities, indicating that the S-enantiomer is strongly favored in forming a stable crystalline hydrate:

- S-Naproxen Hydrate (**S-Nap_RS-Quin_W**): This phase is classified as a channel hydrate, where its water molecules are strongly bound and are arranged within channels. Its dehydration is reversible, yielding a stable anhydrous crystalline phase (**S-Nap_RS-Quin**) with similar cell parameters, suggesting the persistence of the channel structure even after water loss.
- R-Naproxen Hydrate (**R-Nap_RS-Quin_W**): This phase shows weaker water bonding and, upon heating, undergoes an irreversible transformation to an amorphous state, pointing to a reduced intrinsic stability of the R-Nap/RS-Quin chains packing without the stabilizing influence of the crystallization water.

These significant differences in thermal behavior confirm that their crystal packing arrangements are distinct. Furthermore, the differences in thermal and structural stability provide a clear structural rationale for the preferential formation of **S-Nap_RS-Quin_W**; in our opinion, the greater intrinsic structural stability of the **S-Nap_RS-Quin_W** hydrate is the crucial factor governing the selective association observed in the selective crystallization test.

Finally, this work provides valuable data that can be exploited for the rational selection of resolving agents in efficient large-scale chiral separations, contributing to the goal of producing enantiopure APIs.

ASSOCIATED CONTENT

Supporting Information

The Supporting Information is available free of charge at https://pubs.acs.org/doi/10.1021/acs.cgd.5c01538.

CIF files of S-Nap_RS-Quin_W, S-Ibu_RS-Quin, and S-Nap_RS-Cinch; views of fingerprint plots and Hirshfeld surfaces; PXRD patterns; polarimetry analysis results; results of analysis by Fourier Transform Infrared Spectroscopy (FTIR) in Attenuated Total Reflection

https://doi.org/10.1021/acs.cgd.5c01538
Cryst. Growth Des. 2026, 26, 955−969

mode (ATR); table with geometrical parameters for intermolecular interactions; TGA profiles; HSM images; and DSC curves (PDF)

Accession Codes

Deposition Numbers 2499058−2499060 contain the supplementary crystallographic data for this paper. These data can be obtained free of charge via the joint Cambridge Crystallographic Data Centre (CCDC) and Fachinformationszentrum Karlsruhe Access Structures service.

AUTHOR INFORMATION

Corresponding Author

Martina Lippi − *Department of Industrial Engineering, University of Florence, Florence 50139, Italy;* orcid.org/0000-0003-2861-332X; Email: martina.lippi@unifi.it

Authors

Patrizia Rossi − *Department of Industrial Engineering, University of Florence, Florence 50139, Italy;* orcid.org/0000-0002-6316-338X

Meriem Goudjil − *Department of Industrial Engineering, University of Florence, Florence 50139, Italy;* orcid.org/0000-0003-3401-4294

Jacopo Ceccarelli − *Department of Industrial Engineering, University of Florence, Florence 50139, Italy;* Present Address: Publiacqua SpA, Florence 50,100 (Italy); orcid.org/0000-0002-0759-787X

Samuele Ciattini − *Centro di Cristallografia Strutturale, University of Florence, Florence 50019, Italy*

Luca Conti − *Department of Chemistry Ugo Schiff, University of Florence, Florence 50019, Italy;* orcid.org/0000-0002-0402-1293

Andrea Ienco − *CNR-ICCOM, Florence 50019, Italy;* orcid.org/0000-0002-2586-4943

Juliana Morais Missina − *Department of Pharmaceutical Sciences, State University of Ponta Grossa, Ponta Grossa 84030-900, Brazil*

Paola Paoli − *Department of Industrial Engineering, University of Florence, Florence 50139, Italy;* orcid.org/0000-0002-2408-4590

Complete contact information is available at: https://pubs.acs.org/10.1021/acs.cgd.5c01538

Author Contributions

The manuscript was written through contributions of all authors. All authors have given approval to the final version of the manuscript.

Notes

The authors declare no competing financial interest.

ACKNOWLEDGMENTS

Authors would like to thank the Centro di Cristallografia Strutturale (CRIST) of the University of Firenze for the X-ray diffraction facilities. Prof. Camilla Matassini (Department of Chemistry "U. Schiff," University of Florence) is gratefully acknowledged for her assistance in performing the polarimetry analysis of the samples obtained during the selective crystallization test.

ABBREVIATIONS

(S)-(+)-Naproxen, ([(S)-2-(6-methoxynaphthalen-2-yl)-propanoic acid; **(S)-(+)-Ibuprofen**, (S)-2-(4isobutylphenyl)-propanoic acid; **RS-Quinine**, (*R*)-[(2*S*, 4*S*,5*R*)-5-ethenyl-1-azabicyclo[2.2.2]octan-2-yl]-(6-methoxyquinolin-4-yl) methanol; **SR-Cinchonine**, (S)-[(2R, 4S,5R)-5-ethenyl-1-azabicyclo[2.2.2]octan-2-yl)] (quinolin-4-yl) methanol; **RR-Quinine**, (*R*)-[(2*R*, 4*R*,5*R*)-5-ethenyl-1-azabicyclo[2.2.2]-octan-2-yl]-(6-methoxyquinolin-4-yl)methanol; **S-Ibu_RS-Quin**, (S)-2-(4isobutylphenyl)propanoic acid (*R*)-[(2*S*, 4*S*,5*R*)-5-ethenyl-1-azabicyclo[2.2.2]octan-2-yl]-(6-methoxy-quinolin-4-yl) methanol salt; **S-Nap_RS-Quin_W**, (S)-2-(6-methoxynaphthalen-2-yl)propanoic acid (*R*)-[(2*S*, 4*S*,5*R*)-5-ethenyl-1-azabicyclo[2.2.2]octan-2-yl]-(6-methoxyquinolin-4-yl) methanol three hydrate salt; **S-Nap_RS-Quin**: (S)-2-(6-methoxynaphthalen-2-yl)propanoic acid (*R*)-[(2*S*, 4*S*,5*R*)-5-ethenyl-1-azabicyclo[2.2.2]octan-2-yl]-(6-methoxyquinolin-4-yl) methanol salt; **S-Nap_SR-Cinch**, (S)-2-(6-methoxynaphthalen-2-yl)propanoic acid (S)-[(2R, 4S,5R)-5-ethenyl-1-azabicyclo[2.2.2]octan-2-yl)] (quinolin-4-yl) methanol salt; **R-Nap_RS-Quin_W**, (R)-2-(6-methoxynaphthalen-2-yl)-propanoic acid (*R*)-[(2*S*, 4*S*,5*R*)-5-ethenyl-1-azabicyclo[2.2.2]-octan-2-yl]-(6-methoxyquinolin-4-yl) methanol three hydrate salt; XRD, X-ray diffraction; SCXRD, single-crystal X-ray diffraction; PXRD, powder X-ray diffraction; VT-XRD, variable temperature X-ray diffraction; DSC, differential scanning calorimetry; SC, single crystal; TGA, thermogravimetric analysis; HSM, hot stage microscopy

REFERENCES

(1) Senkuttuvan, N.; Komarasamy, B.; Krishnamoorthy, R.; Sarkar, S.; Dhanasekaran, S.; Anaikutti, P. The significance of chirality in contemporary drug discovery-a mini review. *RSC Adv.* **2024**, *14*, 33429−33448.

(2) Fassihi, A. R. Racemates and Enantiomers in Drug Development. *Int. J. Pharm.* **1993**, *92*, 1−14.

(3) Kim, J. H.; Scialli, A. R. Thalidomide: The Tragedy of Birth Defects and the Effective Treatment of Disease. *Toxicol. Sci.* **2011**, *122*, 1−6.

(4) Lee, H. L.; Hung, Y. L.; Amin, A.; Pratama, D. E.; Lee, T. Green and Strategic Approach for Chiral Resolution by Diastereomeric Salt Formation: The Study of Racemic Ibuprofen. *Ind. Eng. Chem. Res.* **2023**, *62*, 1946−1957.

(5) Kar, S.; Sanderson, H.; Roy, K.; Benfenati, E.; Leszczynski, J. Green Chemistry in the Synthesis of Pharmaceuticals. *Chem. Rev.* **2022**, *122*, 3637−3710.

(6) Mane, S. Racemic drug resolution: a comprehensive guide. *Anal.Methods* **2016**, *8*, 7567−7586.

(7) *CRC Handbook of optical resolutions via diastereomeric salt formation*; Kozma, D., Ed.; CRC Press, 2001.

(8) Carvalho, P. S., Jr; Diniz, L. F.; Ayala, A. P. Diastereomeric salts of (*S, S*)-sertraline with l- and d-tartaric acids: an investigation into chiral supramolecular discrimination. *CrystEngComm* **2023**, *25*, 1693−1702.

(9) Bánhegyi, D. F.; Fogassy, E.; Madarász, J.; Pálovics, E. Optical Resolution of Two Pharmaceutical Bases with Various Uses of Tartaric Acid Derivatives and Their Sodium Salts: Racemic Ephedrine and Chloramphenicol Base. *Molecules* **2022**, *27*, 3134.

(10) Lippi, M.; Rossi, P.; Ceccarelli, J.; Milazzo, S.; Missina, J. M.; Ienco, A.; Conti, L.; Chelazzi, L.; Paoli, P. The Same but Not the Same: The Case of (S)-Naproxen/*cis*-1-Amino-2-indanol Chiral Resolution via Diastereomeric Salt Formation. *Cryst. Growth Des.* **2024**, *24*, 1658−1673.

(11) Simon, M.; Shortt, S.; Burke, C.; Bourke, E.; Umerska, A.; Jacob, A.; Davin, S.; Glennon, B. Resolution of Double Salts via Crystallization-Induced Diastereomeric Transformation (CIDT). *Chem. Eng. Technol.* **2025**, *48*, No. e70056.

(12) Kaviani, R.; Jouyban, A.; Shayanfar, A. Chiral resolution methods for racemic pharmaceuticals based on cocrystal formation. *CrystEngComm* **2023**, *25*, 6120−6131.
(13) Rapeenun, P.; Songsermsawad, S.; Boonpalit, K.; Nalaoh, P.; Flood, A. E. Enhancing the Screening Efficiency of Chiral Cocrystals for the Separation of Praziquantel through the Use of Coformer Derivatives. *Cryst. Growth Des.* **2025**, *25*, 790−800.
(14) Rougeot, C.; Hein, J. E. Application of Continuous Preferential Crystallization to Efficiently Access Enantiopure Chemicals. *Org. Process Res. Dev.* **2015**, *19*, 1809−1819.
(15) Buol, X.; Caro Garrido, C.; Robeyns, K.; Tumanov, N.; Collard, L.; Wouters, J.; Leyssens, T. Chiral Resolution of Mandelic Acid through Preferential Cocrystallization with Nefiracetam. *Cryst. Growth Des.* **2020**, *20*, 7979−7988.
(16) Songsermsawad, S.; Nalaoh, P.; Promarak, V.; Flood, A. E. Chiral Resolution of *RS*-Baclofen via a Novel Chiral Cocrystal of *R*-Baclofen and *L*-Mandelic Acid. *Cryst. Growth Des.* **2022**, *22*, 2441−2451.
(17) Springuel, G.; Leyssens, T. Innovative Chiral Resolution Using Enantiospecific Co-Crystallization in Solution. *Cryst. Growth Des.* **2012**, *12*, 3374−3378.
(18) Paoli, P.; Rossi, P.; Chelazzi, L.; Altamura, M.; Fedi, V.; Giannotti, D. Solid State Investigation and Characterization of a Nepadutant Precursor: Polymorphic and Pseudopolymorphic Forms of MEN11282. *Cryst. Growth Des.* **2016**, *16*, 5294−5304.
(19) Paoli, P.; Milazzo, S.; Rossi, P.; Ienco, A. Rationalization of Lattice Thermal Expansion for Beta-Blocker Organic Crystals. *Crystals* **2020**, *10*, 350−361.
(20) Rossi, P.; Paoli, P.; Chelazzi, L.; Conti, L.; Bencini, A. The solid-state structure of the *β*-blocker metoprolol: a combined experimental and in silico investigation. *Acta Crystallogr., Sect. C: Struct. Chem.* **2019**, *75*, 87−96.
(21) Rossi, P.; Paoli, P.; Milazzo, S.; Chelazzi, L.; Ienco, A.; Conti, L. Investigating differences and similarities between betaxolol polymorphs. *Crystals* **2019**, *9*, 509−521.
(22) Rossi, P.; Paoli, P.; Milazzo, S.; Chelazzi, L.; Giovannoni, M. P.; Guerrini, G.; Ienco, A.; Valleri, M.; Conti, L. A combined crystallographic and computational study on dexketoprofen trometamol dihydrate salt. *Crystals* **2020**, *10*, 659−672.
(23) Rossi, P.; Paoli, P.; Chelazzi, L.; Milazzo, S.; Biagi, D.; Valleri, M.; Ienco, A.; Valtancoli, B.; Conti, L. Relationships between Anhydrous and Solvated Species of Dexketoprofen Trometamol: A Solid-State Point of View. *Cryst. Growth Des.* **2020**, *20*, 226−236.
(24) Rossi, P.; Paoli, P.; Ienco, A.; Biagi, D.; Valleri, M.; Conti, L. A new crystal form of the NSAID dexketoprofen. *Acta Crystallogr., Sect. C: Struct. Chem.* **2019**, *75*, 783−792.
(25) Lippi, M.; Goudjil, M.; Rossi, P.; Ceccarelli, J.; Ciattini, S.; Paoli, P. Solvatomorphs of the Dapsone Structurally Related Molecule 3,3′-Diaminodiphenyl Sulfone with Class 2 Residual Solvents: Insights into Their Crystal Structures, Stability, and Transformations. *Cryst. Growth Des.* **2024**, *24*, 9896−9908.
(26) Paoli, P.; Lippi, M.; Milazzo, S.; Rossi, P.; Ceccarelli, J.; Chelazzi, L.; Ienco, A.; Conti, L. Molecular-Level Investigation of Hydrate-Anhydrous Phase Transformations of the Dapsone Structurally Related Compound 3,3′-Diaminophenyl Sulfone. *Cryst. Growth Des.* **2022**, *22*, 7176−7186.
(27) Rossi, P.; Ceccarelli, J.; Milazzo, S.; Paoli, P.; Morais Missina, J.; Ciattini, S.; Ienco, A.; Tuci, G.; Valleri, M.; Giovannoni, M. P.; Guerrini, G.; Conti, L. Nonsteroidal Anti-Inflammatory Drugs-1-Phenylethylamine Diastereomeric Salts: A Systematic Solid-State Investigation. *Cryst. Growth Des.* **2021**, *21*, 6947−6960.
(28) Ha, M.-W.; Paek, S.-M. Recent Advances in the Synthesis of Ibuprofen and Naproxen, Molecules. *Molecules* **2021**, *26*, 4792.
(29) Brogden, R. N.; Pinder, R. M.; Sawyer, P. R.; Speight, T. M.; Avery, G. S. Naproxen: a review of its pharmacological properties and therapeutic efficacy and use. *Drugs* **1975**, *9*, 326−363.
(30) Todd, P. A.; Clissold, S. P. Naproxen. *Drugs* **1990**, *40*, 91−137.
(31) Brogden, R. N.; Heel, R. C.; Speight, T. M.; Avery, G. S. Naproxen up to date: a review of its pharmacological properties and therapeutic efficacy and use in rheumatic diseases and pain states. *Drugs* **1979**, *18*, 241−277.
(32) Duggan, K. C.; Walters, M. J.; Musee, J.; Harp, J. M.; Kiefer, J. R.; Oates, J. A.; Marnett, J. L. Molecular basis for cyclooxygenase inhibition by the non-steroidal anti-inflammatory drug naproxen. *J. Biol. Chem.* **2010**, *285*, 34950−34959.
(33) Papp, L.-A.; Krizbai, S.; Dobó, M.; Hancu, G.; Szabó, Z. I.; Tóth, G. Determination of Chiral Impurity of Naproxen in Different Pharmaceutical Formulations Using Polysaccharide-Based Stationary Phases in Reversed-Phased Mode. *Molecules* **2022**, *27*, 2986.
(34) Landoni, F.; Soraci, A. Pharmacology of chiral compounds: 2-arylpropionic acid derivatives. *Curr. Drug Metab.* **2001**, *2*, 37−51.
(35) Kaur, B.; Singh, P. Inflammation: Biochemistry, cellular targets, anti-inflammatory agents and challenges with special emphasis on cyclooxygenase-2. *Bioorg. Chem.* **2022**, *121*, 105663.
(36) Batra, S.; Bhushan, R. Enantiomeric Resolution of (RS)-Naproxen and Application of (S)Naproxen in the Direct and Indirect Enantioseparation of Racemic Compounds by Liquid Chromatography: A Review. *Current Med. Chem.* **2017**, *24*, 758−780.
(37) Chuong, P. H.; Nguyen, L. A.; He, H. Chiral drugs: an overview. *Int. J. Biomed. Sci.* **2006**, *2*, 85−100.
(38) Agranat, I.; Caner, H.; Caldwell, J. Putting chirality to work: the strategy of chiral switches. *Nat. Rev. Drug Discovery* **2002**, *1*, 753−768.
(39) Foster, R. T.; Jamali, F.; Russell, A. S.; Alballa, S. R. Pharmacokinetics of ketoprofen enantiomers in healthy subjects following single and multipledoses. *J. Pharm. Sci.* **1988**, *77*, 70−73.
(40) Wilen, S. H. Resolving Agents and Resolutions in Organic Chemistry. *Top. Stereochem.* **1971**, *6*, 107−176.
(41) Bitarafan, V.; Anjom-Shoae, J.; Rezaie, P.; Fitzgerald, P. C. E.; Lange, K.; Horowitz, M.; Feinle-Bisset, C. Dose-related effects of intraduodenal quinine on plasma glucose, glucoregulatory hormones and gastric emptying of a nutrient drink, and energy intake, in men with type 2 diabetes: a double-blind, randomised, crossover study. *Diabetologia* **2025**, *68*, 727−738.
(42) Henquin, J. C. Quinine: rediscovery of an old glucose-lowering drug. *Diabetologia* **2025**, *68*, 1355.
(43) Malakar, S.; Sreelatha, L.; Dechtawewat, T.; Noisakran, S.; Yenchitsomanus, P.; Chu, J. J. H.; Limjindaporn, T. Drug repurposing of quinine as antiviral against dengue virus infection. *Virus Res.* **2018**, *255*, 171−178.
(44) Gisselmann, G.; Alisch, D.; Welbers-Joop, B.; Hatt, H. Effects of Quinine, Quinidine and Chloroquine on Human Muscle Nicotinic Acetylcholine Receptors. *Front. Pharmacol* **2018**, *9*, 1339.
(45) Harcher, A.; Ricard, C.; Connolly, D.; Gibbs, I.; Shaw, J.; Butler, J.; Perschbacher, J.; Replogle, L.; Eide, M.; Grissom, M.; O'Neal, O.; Nguyen, Q.; Nguyen, V. H.; Hunnicutt, M.; Mahmoud, R.; Dhakal, S. Fluorescence Analysis of Quinine in Commercial Tonic Waters. *Methods Protoc* **2025**, *8*, 5.
(46) Kacprzak, K.; Gawronski, J. Resolution of Racemates and Enantioselective Analytics by Cinchona Alkaloids and Their Derivatives. *Cinchona Alkaloids Synth. Catal.* **2009**, 419−469.
(47) Gal, G. Louis Pasteur, Chemist: An Account of His Studies of Cinchona Alkaloids. *Helvetica* **2019**, *102*, No. e1800226.
(48) Liu, W., *Resolution at Large Scale: Case Studies. Handbook of Chiral Chemistry*. 2 nd; ed., David, A., Ed., Taylor & Francis, 2006.
(49) Harrington, P. J.; Lodewijk, E. Twenty years of Naproxen Technology. *Org. Process Res. & Devel.* **1997**, *1*, 72−76.
(50) Hu, G.; Lu, Q.; Mao, X.; Qin, S.; Yang, K.; Ge, L. Enantioselective extraction of ibuprofen enantiomers using quinine-terminated tetra-arm PEGs as a recyclable chiral selector. *Sust. Chem. & Pharm.* **2025**, *45*, 102009.
(51) Groom, C. R.; Bruno, I. J.; Lightfoot, M. P.; Ward, S. C. The Cambridge Structural Database. *Acta Crystallogr.* **2016**, *B72*, 171−179.
(52) Schlesinger, C.; Tapmeyer, L.; Gumbert, S. D.; Prill, D.; Bolte, M.; Schmidt, M. U.; Saal, C. Absolute Configuration of Pharmaceutical Research Compounds Determined by X-ray Powder Diffraction. *Angew. Chem., Int. Ed.* **2018**, *57*, 9150−9153.
(53) Bruker. *Apex 4*; Bruker AXS Inc.: Madison, Wisconsin, USA, 2021

https://doi.org/10.1021/acs.cgd.5c01538
Cryst. Growth Des. 2026, 26, 955−969

(54) Sheldrick, G. M. *Program for Absorption Correction of Area Detector Frames*; BRUKER AXS Inc.: 5465 East Cheryl Parkway, Madison, WI 53711−5373 USA
(55) Sheldrick, G. M. SHELXT-Integrated space-group and crystal-structure determination. *Acta Crystallogr A Found Adv* **2015**, *71*, 3−8.
(56) Sheldrick, G. M. Crystal structure refinement with SHELXL. *Acta Crystallogr., Sect. C: Struct. Chem.* **2015**, *71*, 3−8.
(57) Dolomanov, O. V.; Bourhis, L. J.; Gildea, R. J.; Howard, J. A.; Puschmann, H. OLEX2: a complete structure solution, refinement and analysis program. *J. Appl. Crystallogr.* **2009**, *42* (2), 339−341.
(58) Macrae, C. F.; Bruno, I. J.; Chisholm, J. A.; Edgington, P. R.; McCabe, P.; Pidcock, E.; Rodriguez-Monge, L.; Taylor, R.; van de Streek, J.; Wood, P. A. Mercury CSD 2.0 - New Features for the Visualization and Investigation of Crystal Structures. *J. Appl. Crystallogr.* **2008**, *41*, 466−470.
(59) Altomare, A.; Cuocci, C.; Giacovazzo, C.; Moliterni, A.; Rizzi, R.; Corriero, N.; Falcicchio, a. EXPO2013: a kit of tools for phasing crystal structures from powder data". *J. Appl. Crystallogr.* **2013**, *46*, 1231−1235.
(60) Faddegon, B.; Ramos-Mendez, J.; Schuemann, J.; McNamara, A.; Shin, J.; Perl, J.; Paganetti, H. The TOPAS Tool for Particle Simulation, a Monte Carlo Simulation Tool for Physics, Biology and Clinical Research. *Phys. Med.* **2020**, *72*, 114−121.
(61) *STARe, Thermal Analysis Software*. Mettler - Toledo Int. Inc - Sonnenbergstrasse 74 - CH-8603 Schwerzenbahc, Switzerland.
(62) Spackman, P. R.; Turner, M. J.; McKinnon, J. J.; Wolff, S. K.; Grimwood, D. J.; Jayatilaka, D.; Spackman, M. A. CrystalExplorer: a program for Hirshfeld surface analysis, visualization and quantitative analysis of molecular crystals. *J. Appl. Crystallogr.* **2021**, *54*, 1006−1011.
(63) Kashino, S.; Haisa, M. Structure of quinidine, $C_{20}H_{24}N_2O_2$. *Acta Crystallogr., Sect.C: Cryst.Struct.Commun.* **1983**, *39*, 310.
(64) Brandenburg, J. G.; Caldeweyher, E.; Grimme, S. Screened Exchange Hybrid Density Functional for Accurate and Efficient Structures and Interaction Energies. *Phys. Chem. Chem. Phys.* **2016**, *18*, 15519−15523.
(65) Dovesi, R.; Erba, A.; Orlando, R.; Zicovich-Wilson, C. M.; Civalleri, B.; Maschio, L.; Rérat, M.; Casassa, S.; Baima, J.; Salustro, S.; Kirtman, B. Quantum-Mechanical Condensed Matter Simulations with CRYSTAL. *Wiley Interdiscip. Rev.: Comput. Mol. Sci.* **2018**, *8*..
(66) https://www.piketech.com/ (accessed 24th December 2025).
(67) Etter, M. C.; MacDonald, J. C.; Bernstein, J. Graph-set analysis of hydrogen-bond patterns in organic crystals. *Acta Crystallogr., Sect. B: Struct. Sci.* **1990**, *46*, 256−262.
(68) Among the 85 deposited structures featuring the paired carboxylate anion-quinine/cinchonine cation, 33 exhibit the motif.
(69) Desiraju, G. R.; Steiner, T. The Weak Hydrogen Bond in Structural Chemistry and Biology. *J. Am. Chem. Soc.* **2000**, 191−192.
(70) Morris, K. R. *Polymorphism in Pharmaceutical Solids*; Brittain, H. G., Ed.; Marcel Dekker: New York, 1999; pp 125−181..
(71) Byrn, S. R.; Zografi, G.; Chen, X. *Solid-State Properties of Pharmaceutical Materials*; Wiley: Hoboken, NJ., 2017.
(72) Vippagunta, S. R.; Brittain, H. G.; Grant, D. J. W. Crystalline solids. *Adv. Drug Delivery Rev.* **2001**, *48*, 3−26.
(73) Oleksyn, B.; Lebioda, L.; Ciechanowicz-Rutkowska, M. The molecular and crystal structure of the alkaloid cinchonine. *Acta Crystallogr. Sect. B Struct. Crystallogr. Cryst. Chem.* **1979**, *B35*, 440−444.
(74) Marchand, P.; Lefèbvre, L.; Querniard, F.; Cardinaël, P.; Perez, G.; Counioux, J. J.; Coquerel, G.; Perez, G.; Counioux, J. J.; Counioux, J. J.; Coquerel, G. Diastereomeric Resolution Rationalized by Phase Diagrams under the Actual Conditions of the Experimental Process. *Tetrahedron: Asymmetry* **2004**, *15*, 2455−2465.
(75) Fogassy, K.; Harmat, V.; Böcskei, Z.; Tárkányi, G.; Tőke, L.; Faigl, F. Efficient synthesis and resolution of (±)-1-[2-carboxy-6-(trifluoromethyl)phenyl]pyrrole-2-carboxylic acid, Tetrahedra. *Tetrahedron Asymmetry* **2000**, *11*, 4771−4780.
(76) Carvalho, P. S.; Tenorio, J. C.; Diniz, L. F. Double Salt Formation on Diastereoisomeric Crystallization of Mefloquine with Propionic and Succinic Acid Derivatives: A Structural Study of Chiral Non-discrimination. *Cryst. Growth Des.* **2025**, *25*, 1315−1329.
(77) Bereczki, L.; Zodge, A.; Kőrösi, M.; Holczbauer, T.; De, S.; Székely, E.; Bombicz, P. A bug in enantiomer separation: double salt formation - diastereomeric and double salt structures of 1-cyclohexylethylammonium 2- and 4-chloromandelate. *CrystEngComm* **2021**, *23*, 5367−5376.

https://doi.org/10.1021/acs.cgd.5c01538
Cryst. Growth Des. 2026, 26, 955−969